Photochemical and Photobiological Properties of Pyridyl-Pyrazol(in)e-based Ruthenium (II) Complexes with Submicromolar Cytotoxicity for Phototherapy

Dmytro Havrylyuk, David K. Heidary, Yang Sun,[#] Sean Parkin, and Edith C. Glazer**
Department of Chemistry, University of Kentucky, 505 Rose Street, Lexington, Kentucky 40506, United States
[#] Current address: Department of Medicine, Rheumatology, University of California, 513 Parnassus Ave, San Francisco, California 94143, United States

Supplementary Information

1. **Table S1:** HPLC gradient used for analysis of compound purity and photochemical products.

Time (min)	% dH_2O (0.1% formic acid)	% CH_3CN (0.1% formic acid)
0	98	2
2	95	5
5	95	5
10	90	10
20	90	10
25	70	30
30	40	60
35	5	95
40	98	2
45	98	2

2. Additional Schemes and Figures.

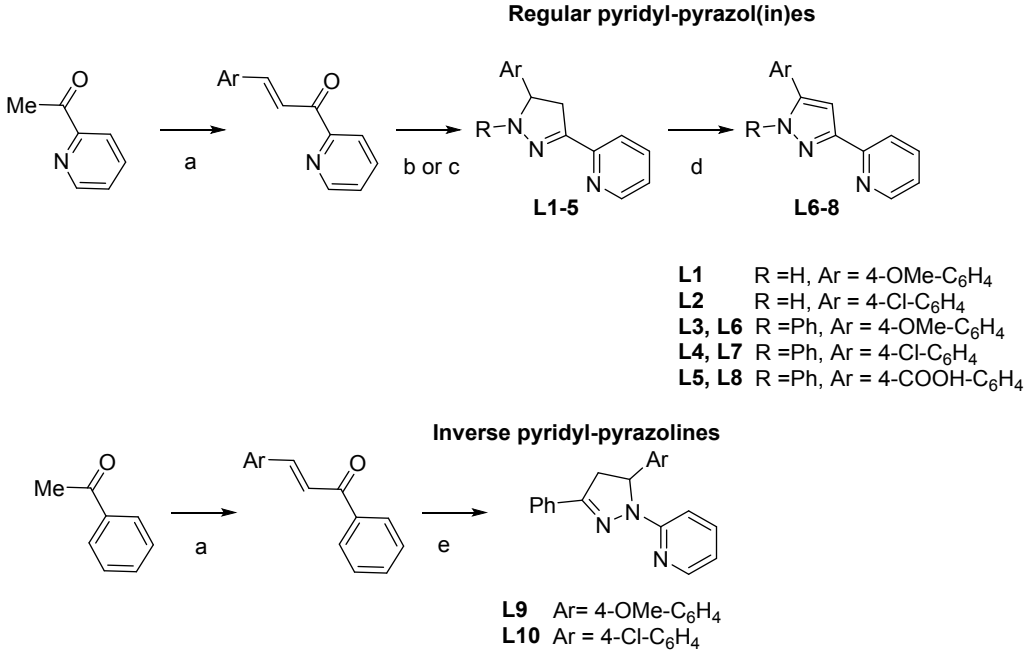

Scheme S1. Synthesis of "regular" (**L1-8**) and "inverse" (**L9, 10**) pyridyl-pyrazol(in)e ligands. Reagents, and conditions: (a) ArCHO (1.1 equiv), KOH (0.1 equiv), EtOH, RT 1–3 h; (b) hydrazine hydrate (1.0 equiv), EtOH, reflux 0.5 h; (c) phenyl hydrazine (2 equiv), AcOH, reflux 3 h; (d) MnO_2 (13.0 equiv), AcOH/DCM 2:1, reflux 24 h; (e) pyrid-2-yl hydrazine (1.2 equiv), NaOH (2.0 equiv), EtOH, reflux 4 h.

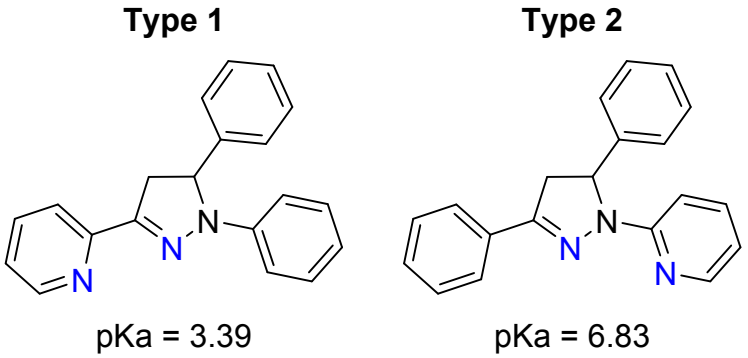

Chart S1. pKa values for model "regular" pyridyl-pyrazoline (Type 1) and "inverse" pyridyl-pyrazoline (Type 2), predicted by SciFinder. Coordinating atoms are colored blue.

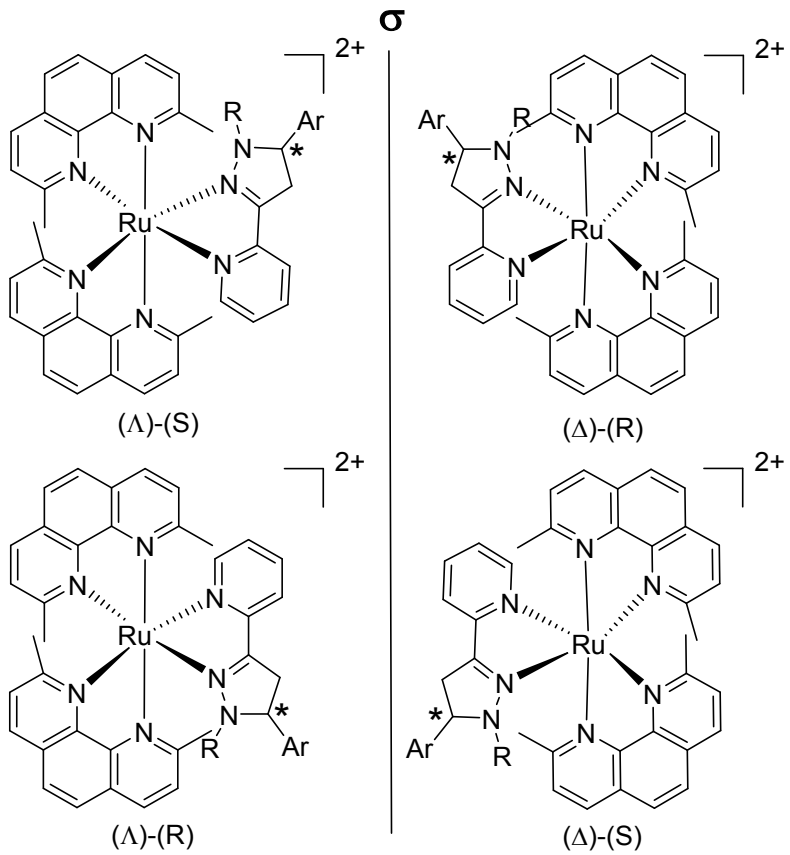

Figure S1. Stereoisomers of Ru(II) complexes with pyridine-pyrazoline ligands

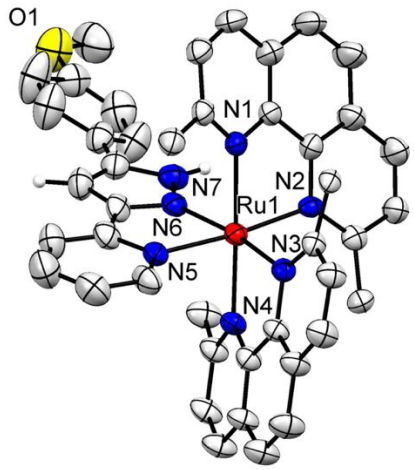

Figure S2. Crystal structures of **1a**. Ellipsoids are drawn to 50% probability. Hydrogen atoms were omitted for clarity.

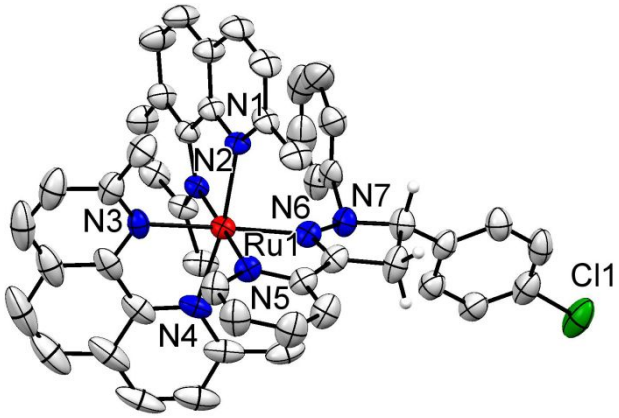

Figure S3. Crystal structures of **4**. Ellipsoids are drawn to 50% probability. Hydrogen atoms were omitted for clarity.

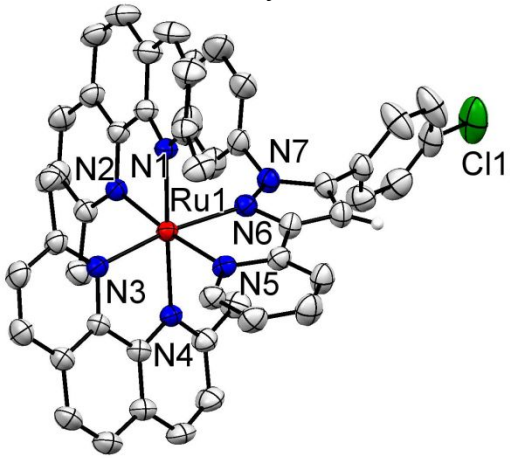

Figure S4. Crystal structures of **8**. Ellipsoids are drawn to 50% probability. Hydrogen atoms were omitted for clarity.

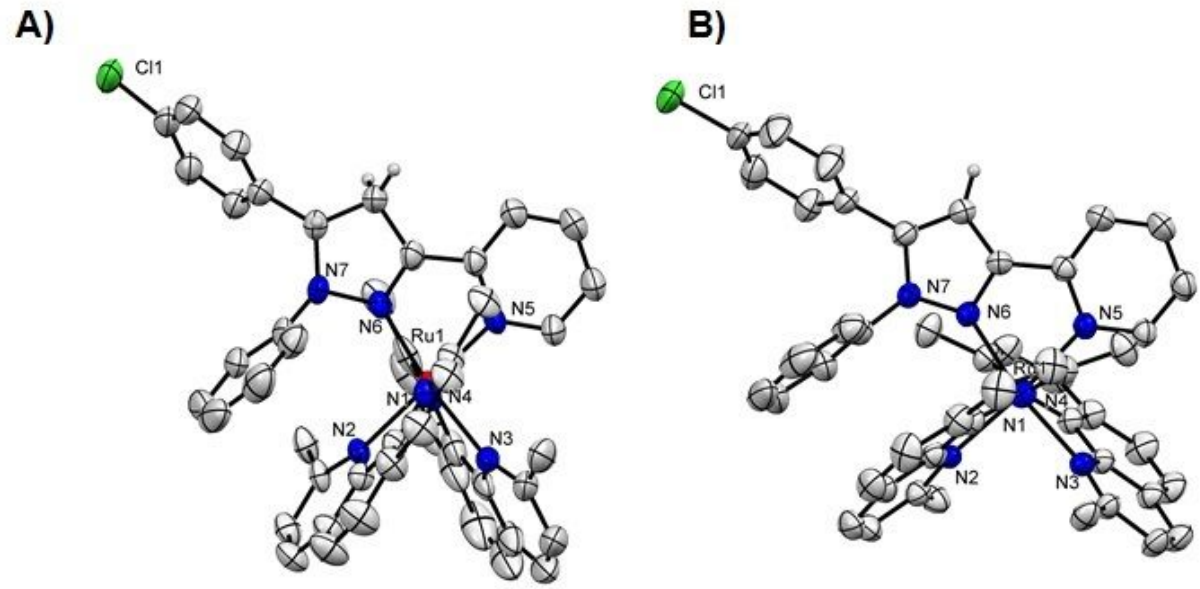

Figure S5. Crystal structures of **4** (A) and **8** (B) highlighting the bend angles of the dmphen coligands. Ellipsoids are drawn to 50% probability. Hydrogen atoms were omitted for clarity.

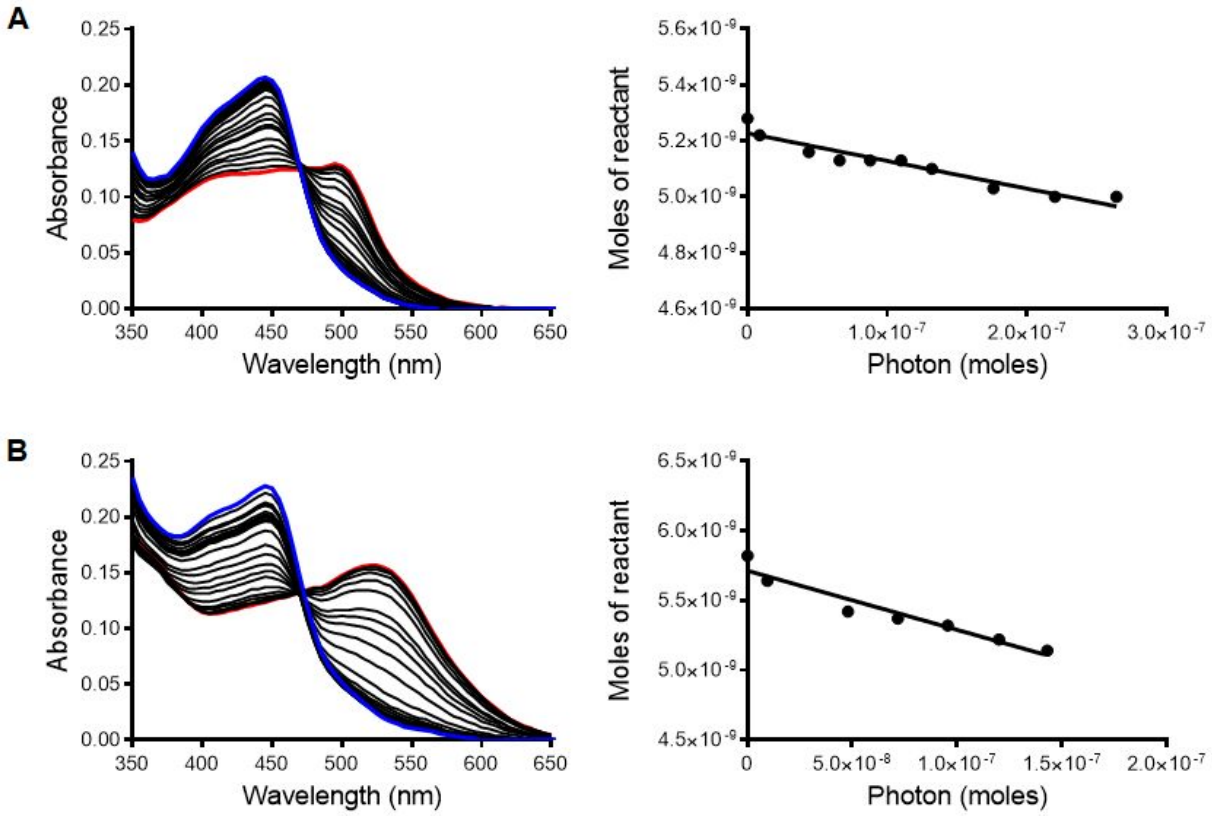

Figure S6. Photoejection of **1** in water (A) and Opti-MEM (B) followed by UV/vis absorption over the course of 0 (blue line) to 240 (red line) min irradiation with 470 nm light. Right column: liner regression for moles of reactant vs. moles of photons absorbed for complex **1**.

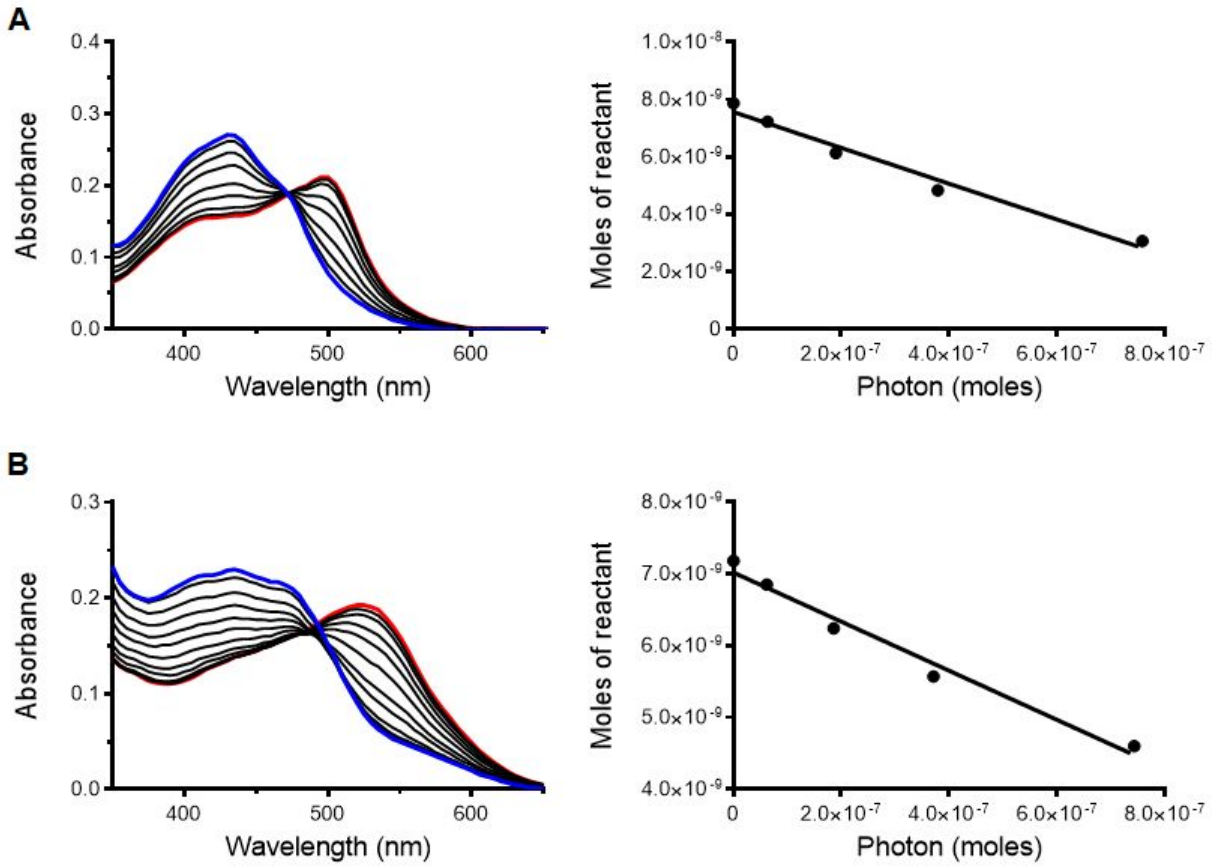

Figure S7. Photoejection of **1a** in water (A) and Opti-MEM (B) followed by UV/vis absorption over the course of 0 (blue line) to 30 (red line) min irradiation with 470 nm light. Right column: liner regression for moles of reactant vs. moles of photons absorbed for complex **1a**.

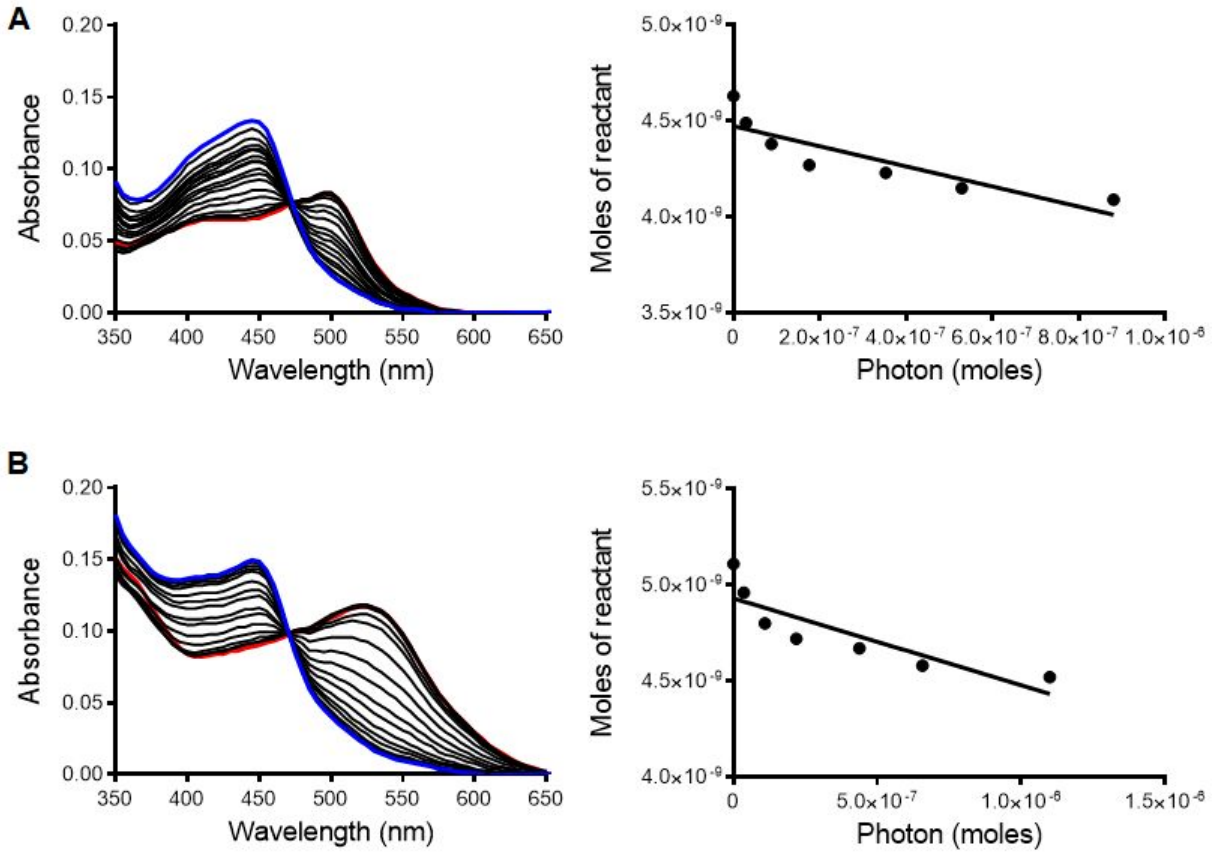

Figure S8. Photoejection of **2** in water (A) and Opti-MEM (B) followed by UV/vis absorption over the course of 0 (blue line) to 240 (red line) min irradiation with 470 nm light. Right column: liner regression for moles of reactant vs. moles of photons absorbed for complex **2**.

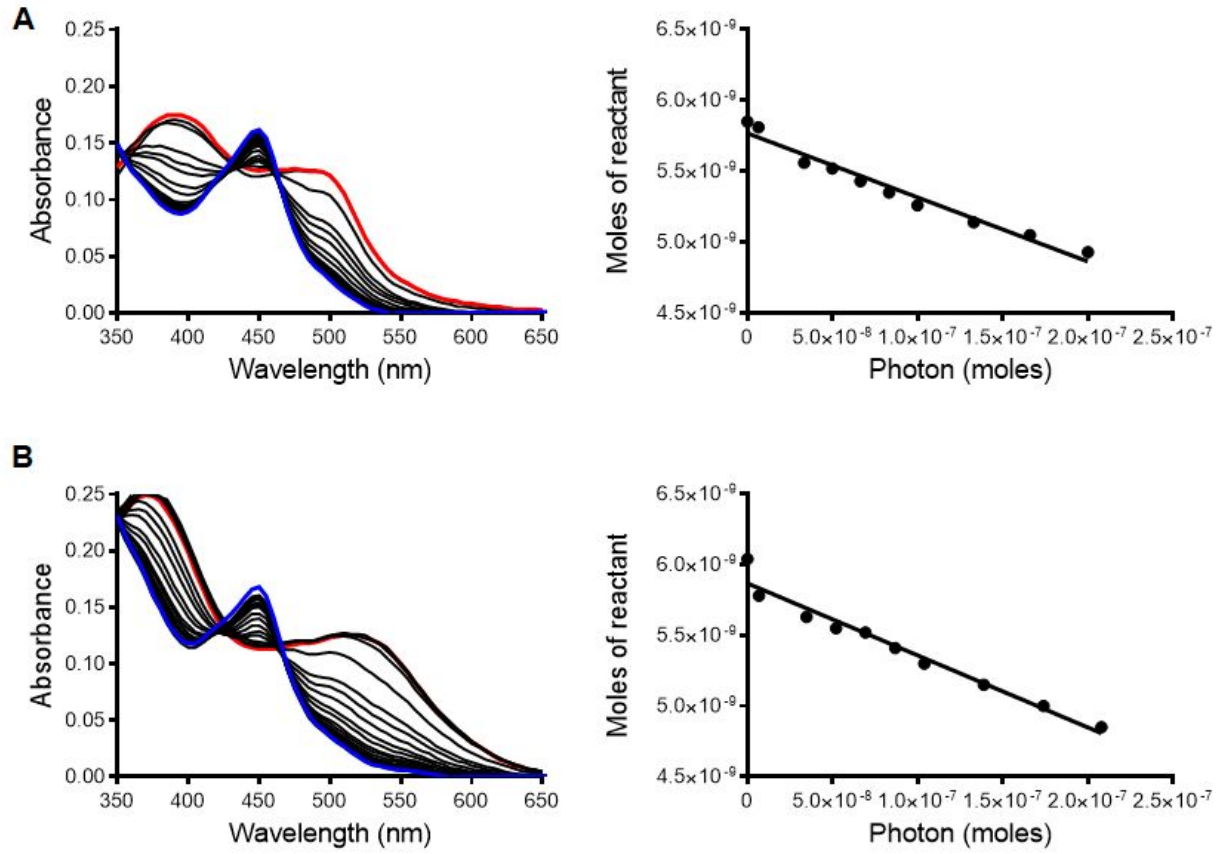

Figure S9. Photoejection of **3** in water (A) and Opti-MEM (B) followed by UV/vis absorption over the course of 0 (blue line) to 60 (red line) min irradiation with 470 nm light. Right column: liner regression for moles of reactant vs. moles of photons absorbed for complex **3.**

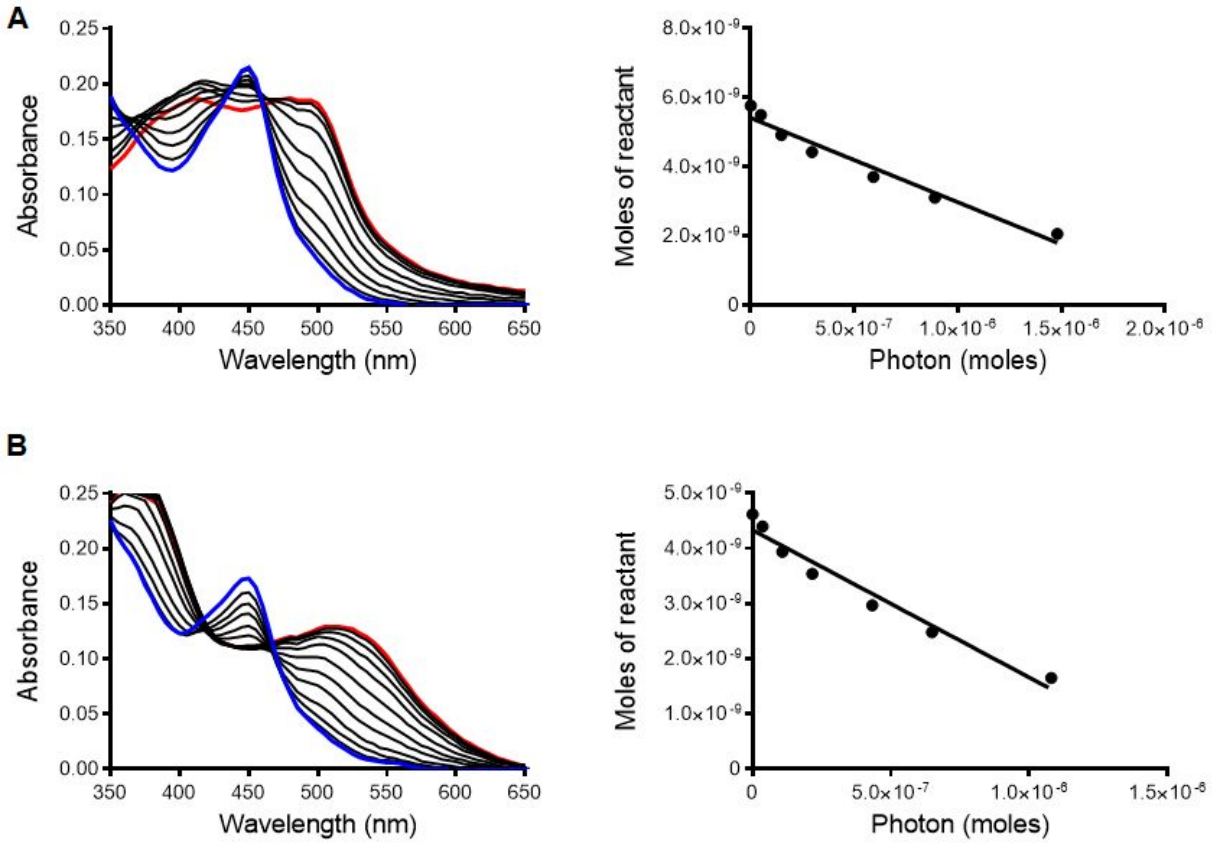

Figure S10. Photoejection of **4** in water (A) and Opti-MEM (B) followed by UV/vis absorption over the course of 0 (blue line) to 60 (red line) min irradiation with 470 nm light. Right column: liner regression for moles of reactant vs. moles of photons absorbed for complex **4**.

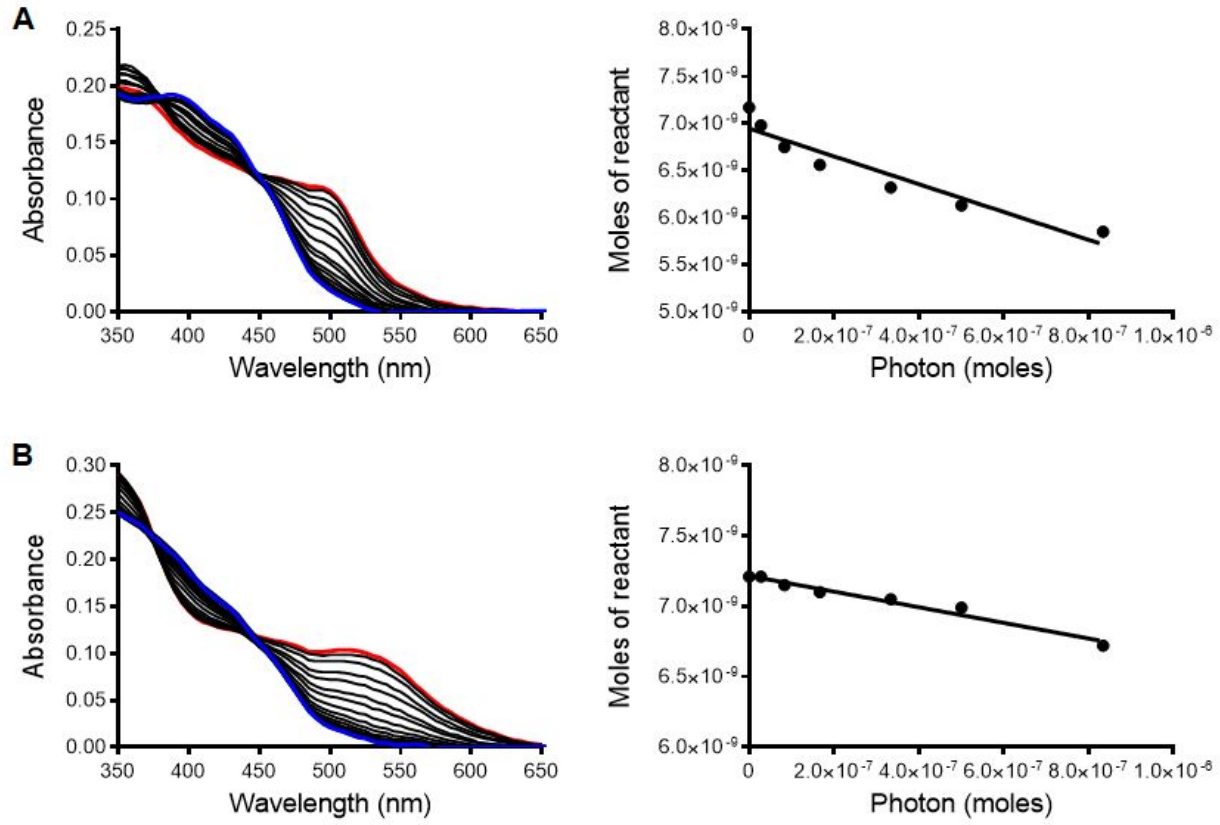

Figure S11. Photoejection of **5** in water (A) and Opti-MEM (B) followed by UV/vis absorption over the course of 0 (blue line) to 300 (red line) min irradiation with 470 nm light. Right column: liner regression for moles of reactant vs. moles of photons absorbed for complex **5**.

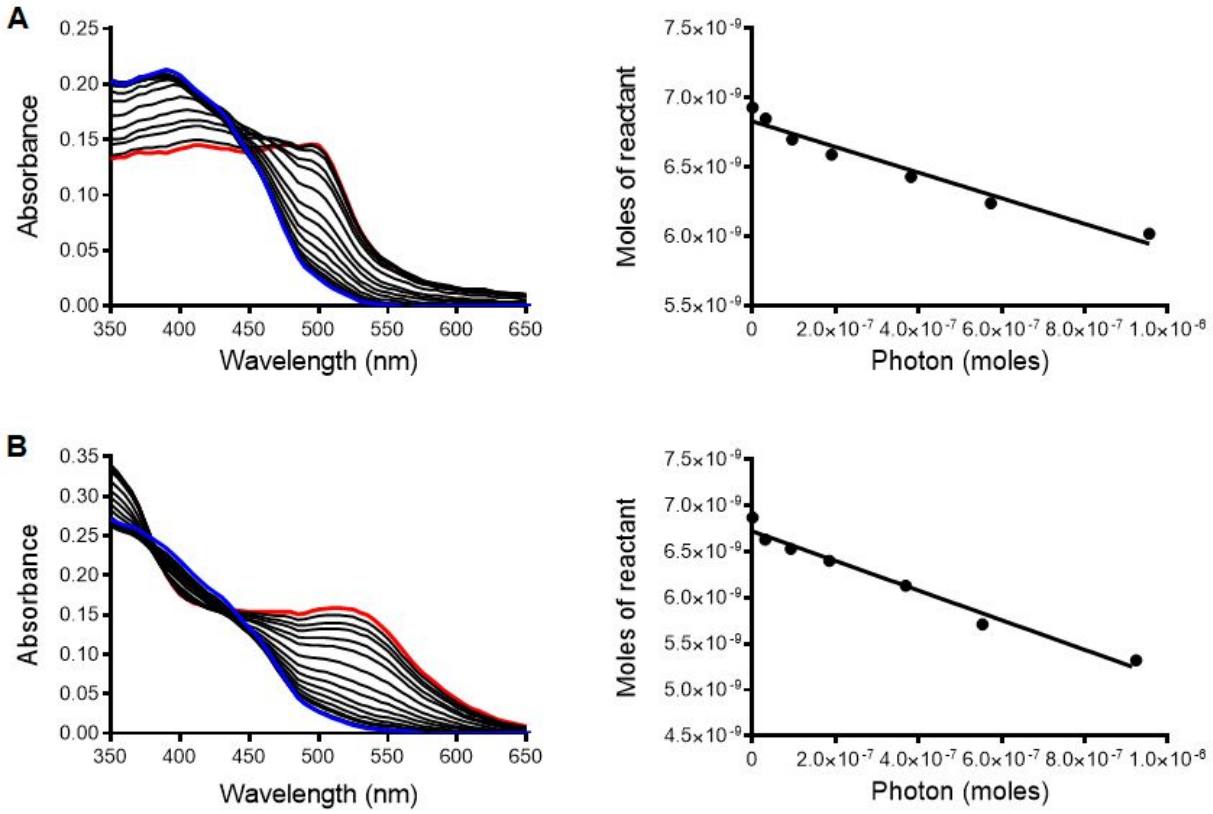

Figure S12. Photoejection of **6** in water (A) and Opti-MEM (B) followed by UV/vis absorption over the course of 0 (blue line) to 300 (red line) min irradiation with 470 nm light. Right column: liner regression for moles of reactant vs. moles of photons absorbed for complex **6**.

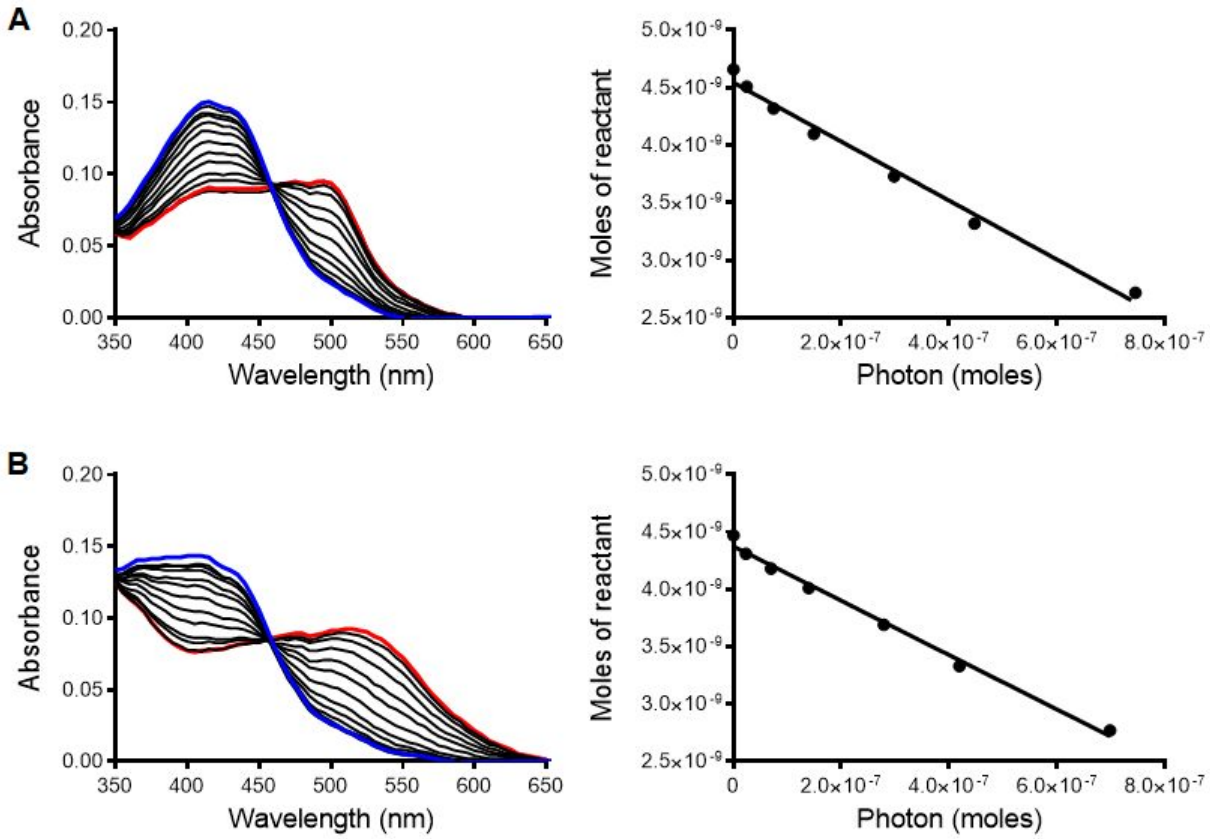

Figure S13. Photoejection of **7** in water (A) and Opti-MEM (B) followed by UV/vis absorption over the course of 0 (blue line) to 90 (red line) min irradiation with 470 nm light. Right column: liner regression for moles of reactant vs. moles of photons absorbed for complex **7**.

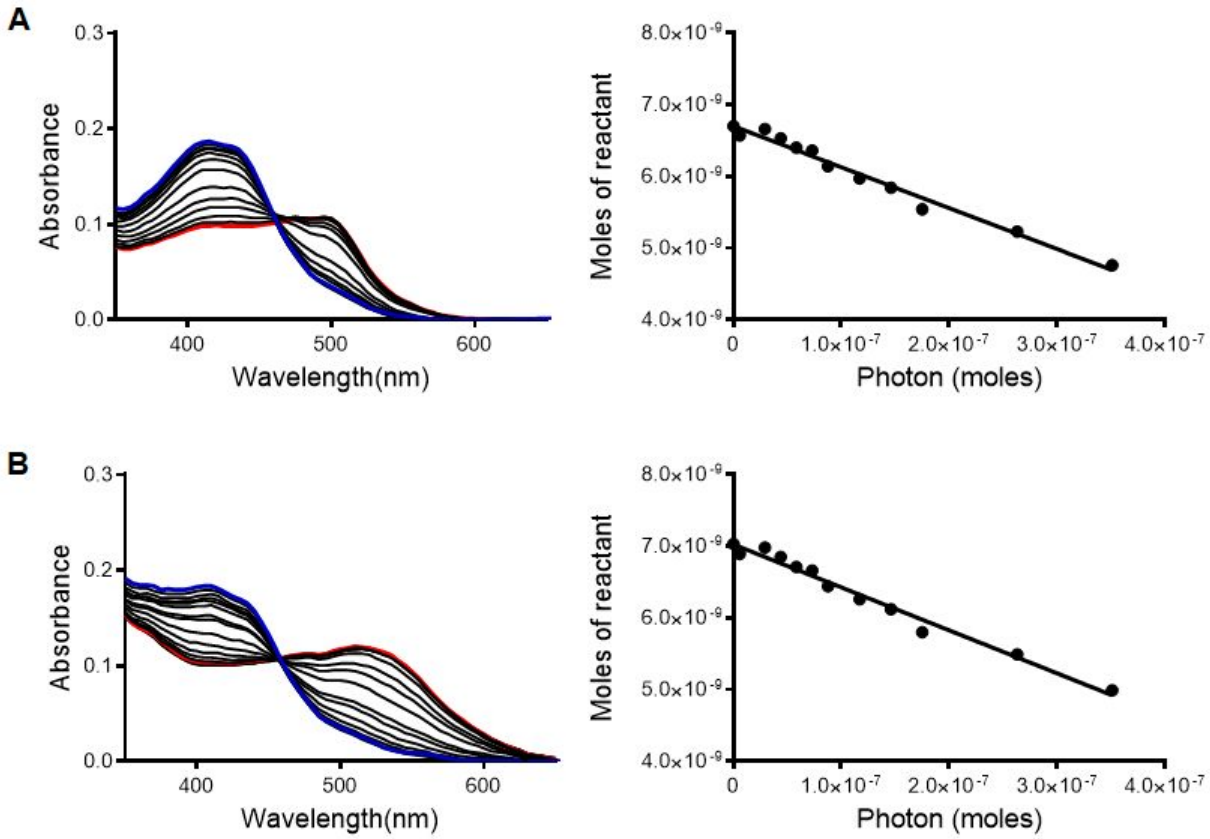

Figure S14. Photoejection of **11** in water (A) and Opti-MEM (B) followed by UV/vis absorption over the course of 0 (blue line) to 30 (red line) min irradiation with 470 nm light. Right column: liner regression for moles of reactant vs. moles of photons absorbed for complex **11**.

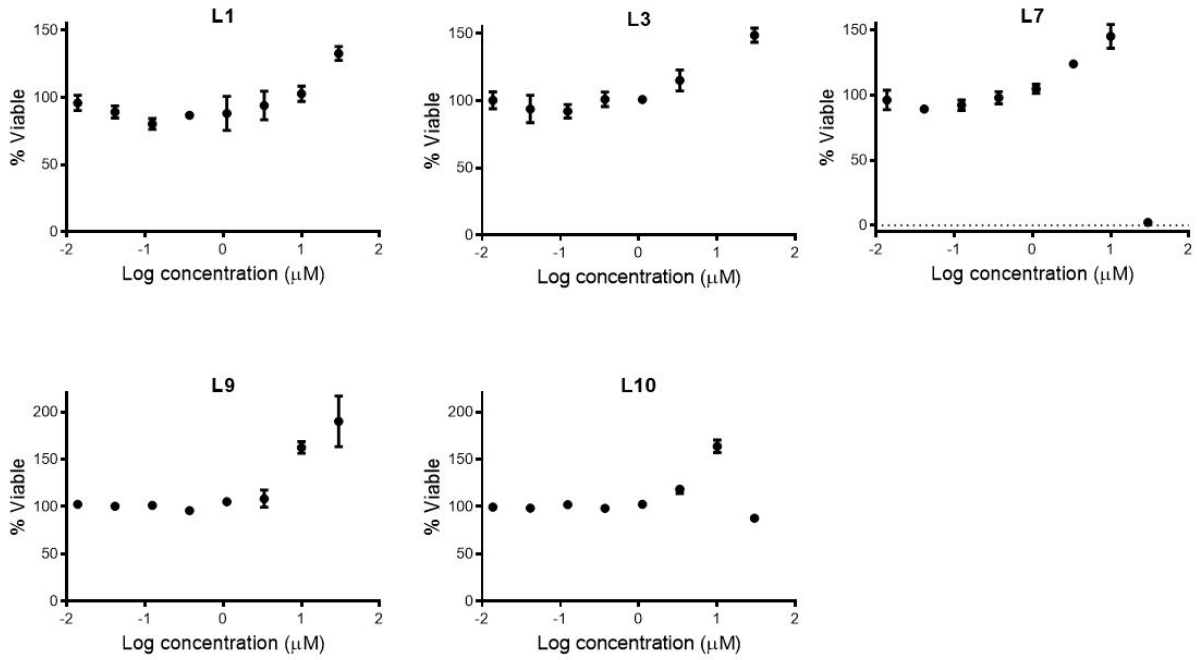

Figure S15. Cytotoxicity dose responses of ligands **L1, L3, L7, L9**, and **L10** (see Scheme S1) on HL60 cells. The ligands are not toxic, but some do have effects where they enhance cell growth at higher concentrations. We have observed this in some cases for other ligands, and can only postulate that the ligands act as ionophores for some metals that aid in cell growth.

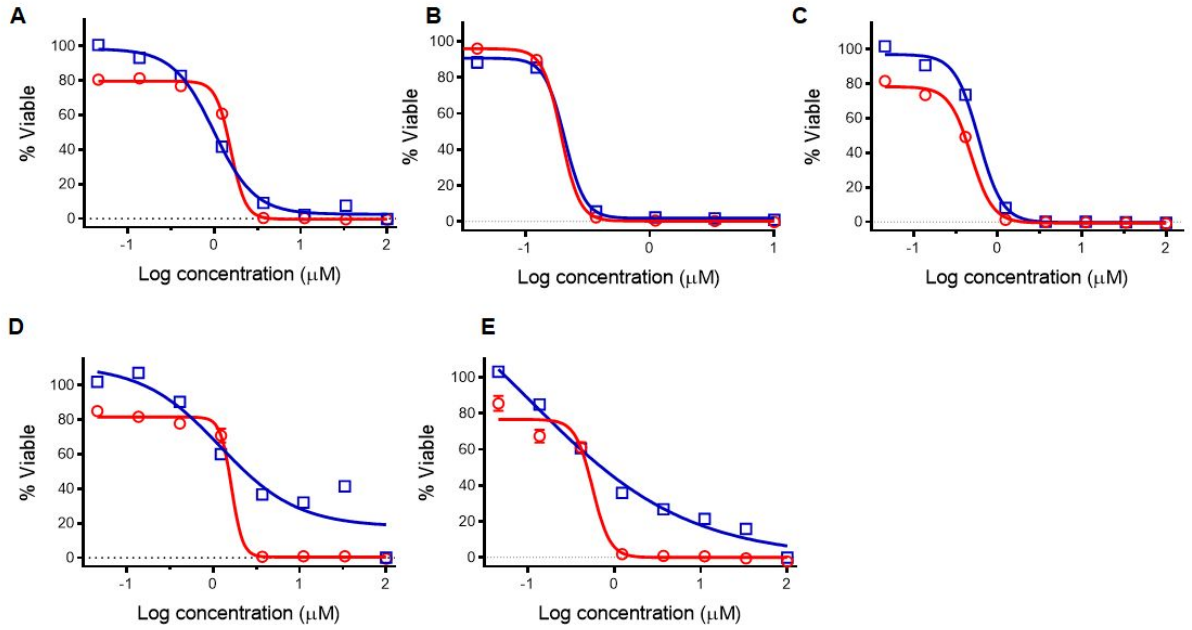

Figure S16. Cytotoxicity dose responses of strained ruthenium complexes on HL60 cells: A) **1**; B) **1a**; C) **2**; D) **3,** E) **4** . Dark conditions (squares, blue line); irradiated samples, 1 min >450 nm light (circles, red line). (n = 3).

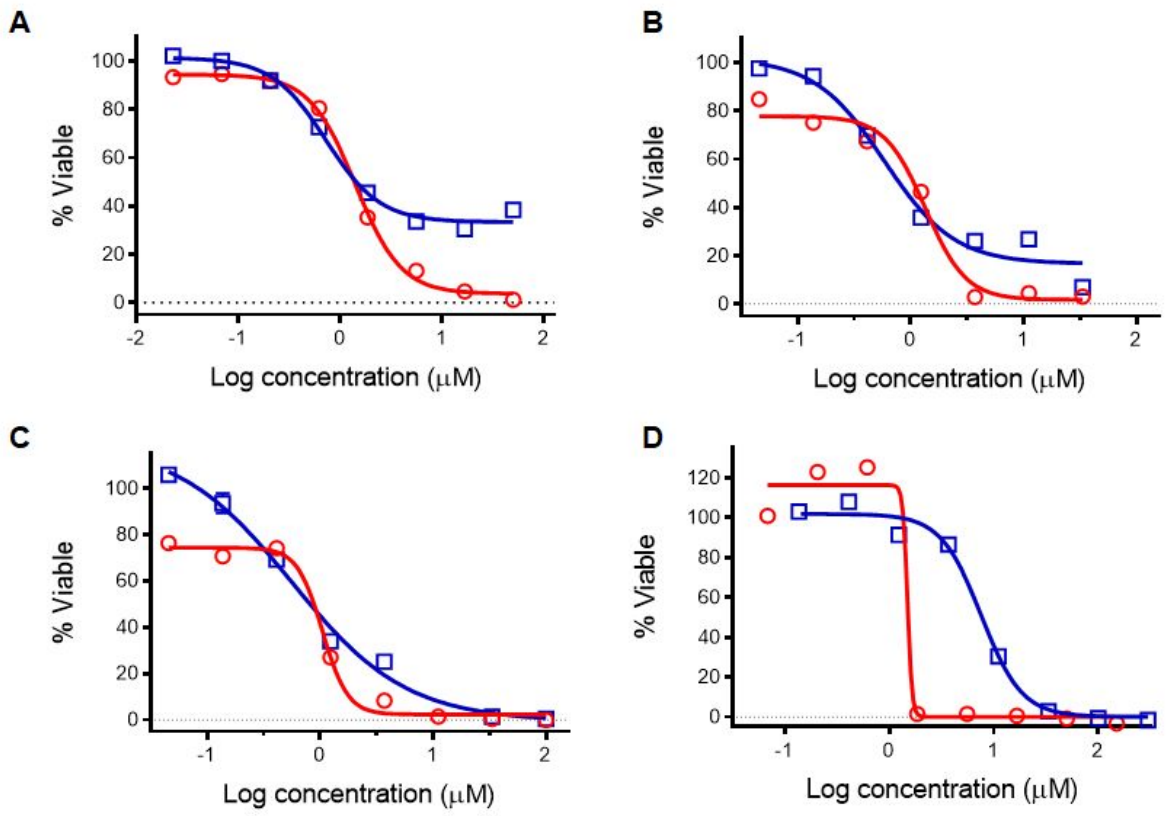

Figure S17. Cytotoxicity dose responses of strained ruthenium complexes on HL60 cells: A) **5**; B) **6**; C) **7**; D) **8**. Dark conditions (squares, blue line); irradiated samples, 1 min >450 nm light (circles, red line). (n = 3).

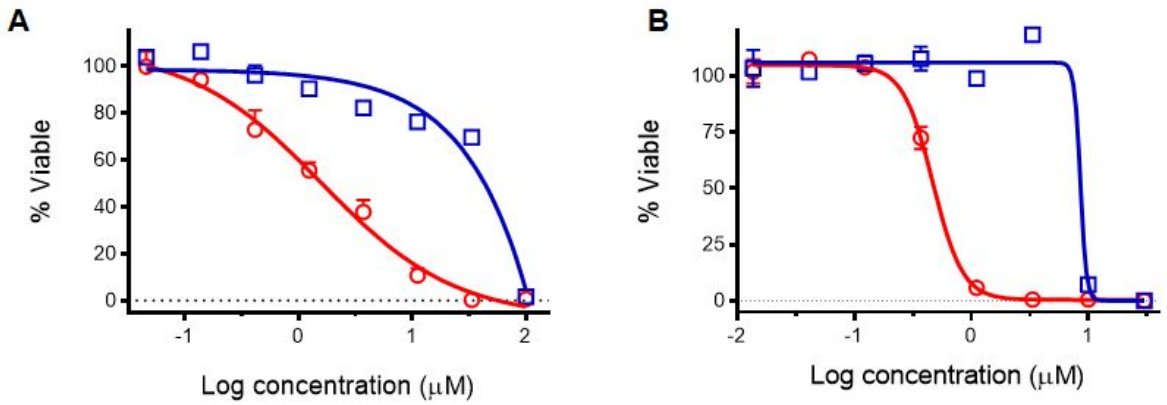

Figure S18. Cytotoxicity dose responses of unstrained ruthenium complexes on HL60 cells: A) **9**; B) **10**. Dark conditions (squares, blue line); irradiated samples, 1 min >450 nm light (circles, red line). (n = 3).

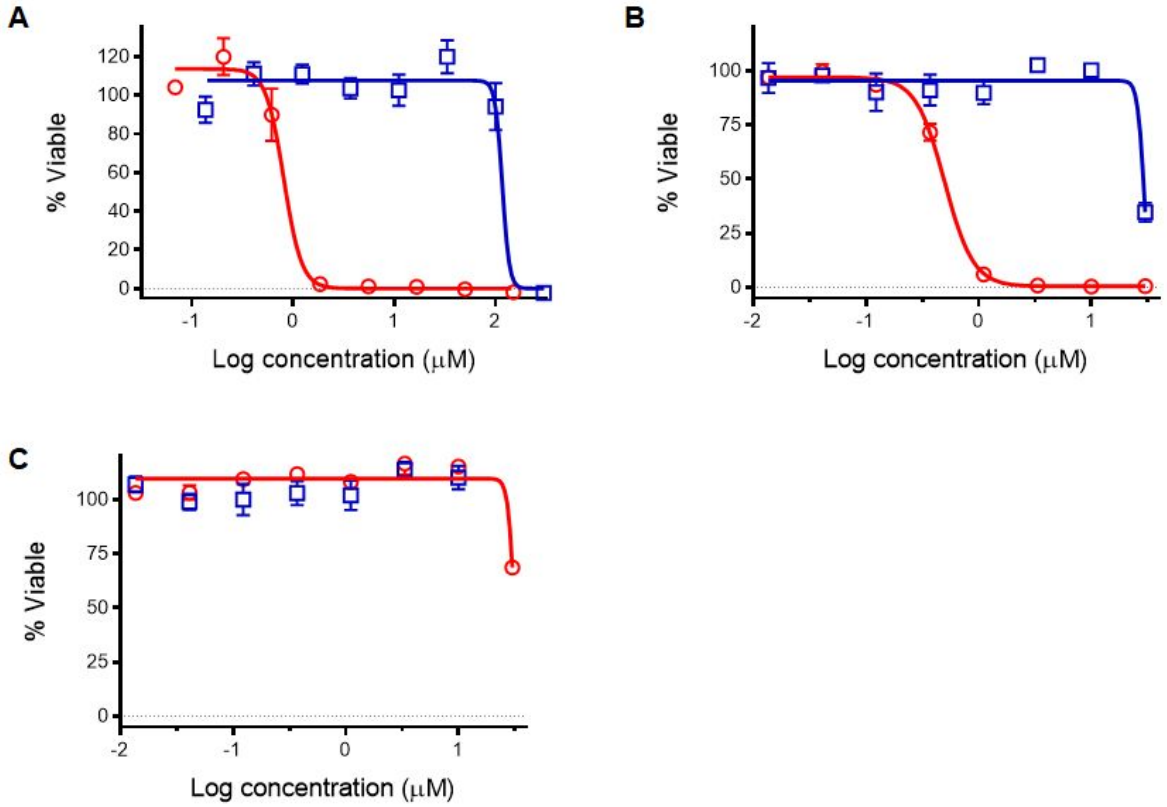

Figure S19. Cytotoxicity dose responses of ruthenium complexes **11** (A) and **12** (B) compared with parent pyridyl-pyrazole ligand (C) on HL60 cells. Dark conditions (squares, blue line); irradiated samples, 1 min >450 nm light (circles, red line). (n = 3).

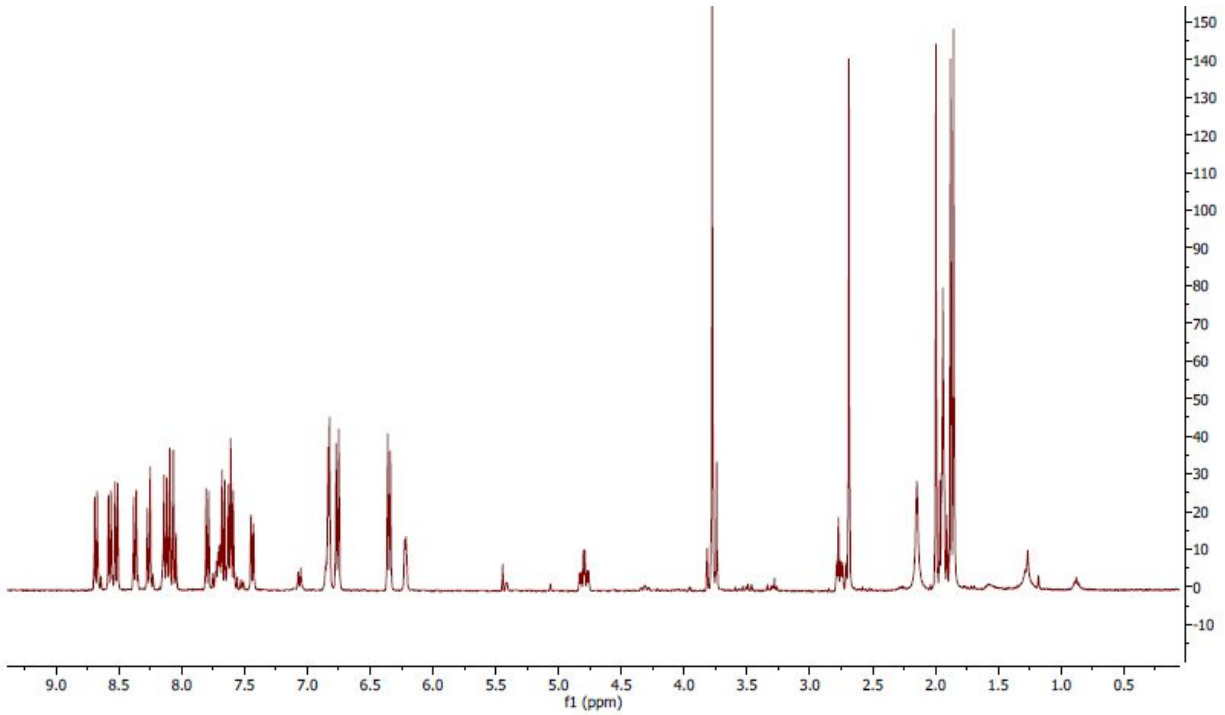

Figure S20. ^{1}H NMR of **1** in CD_3CN.

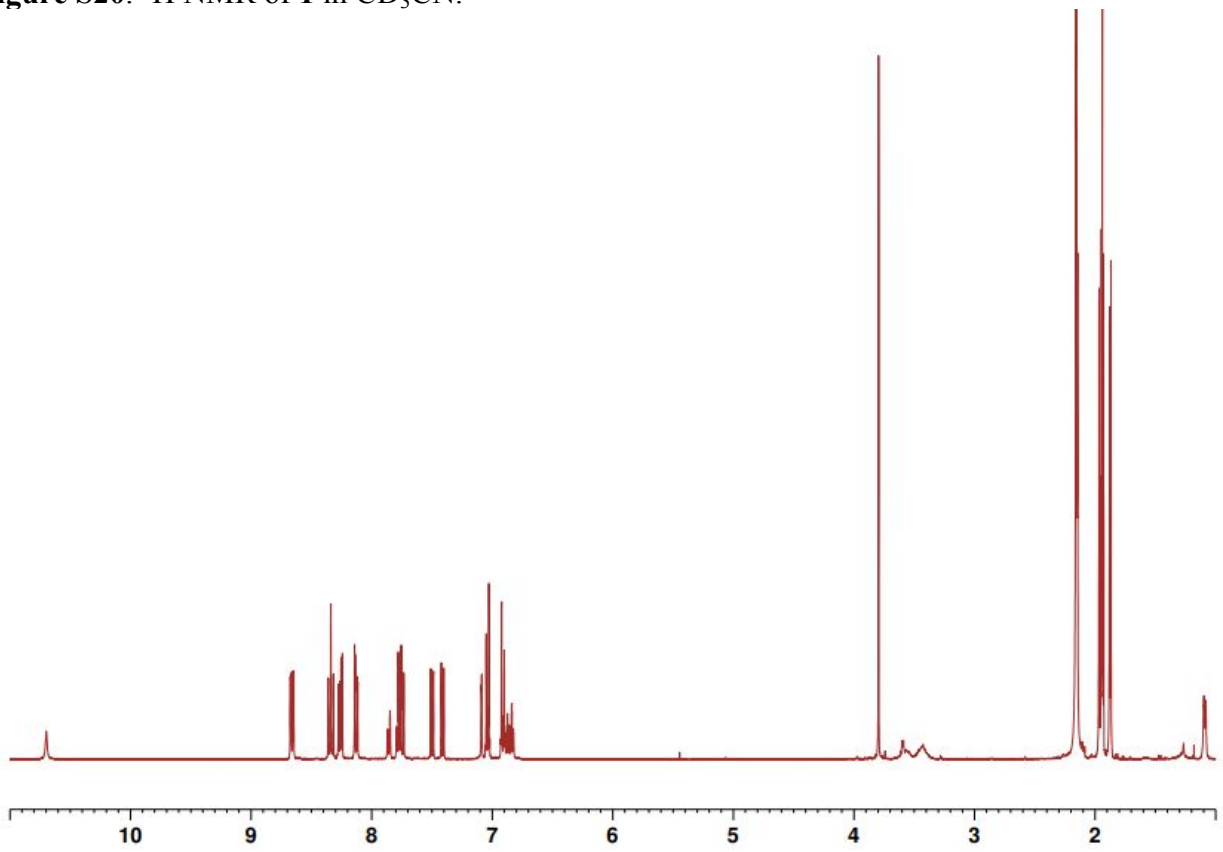

Figure S21. ^{1}H NMR of **1a** in CD_3CN.

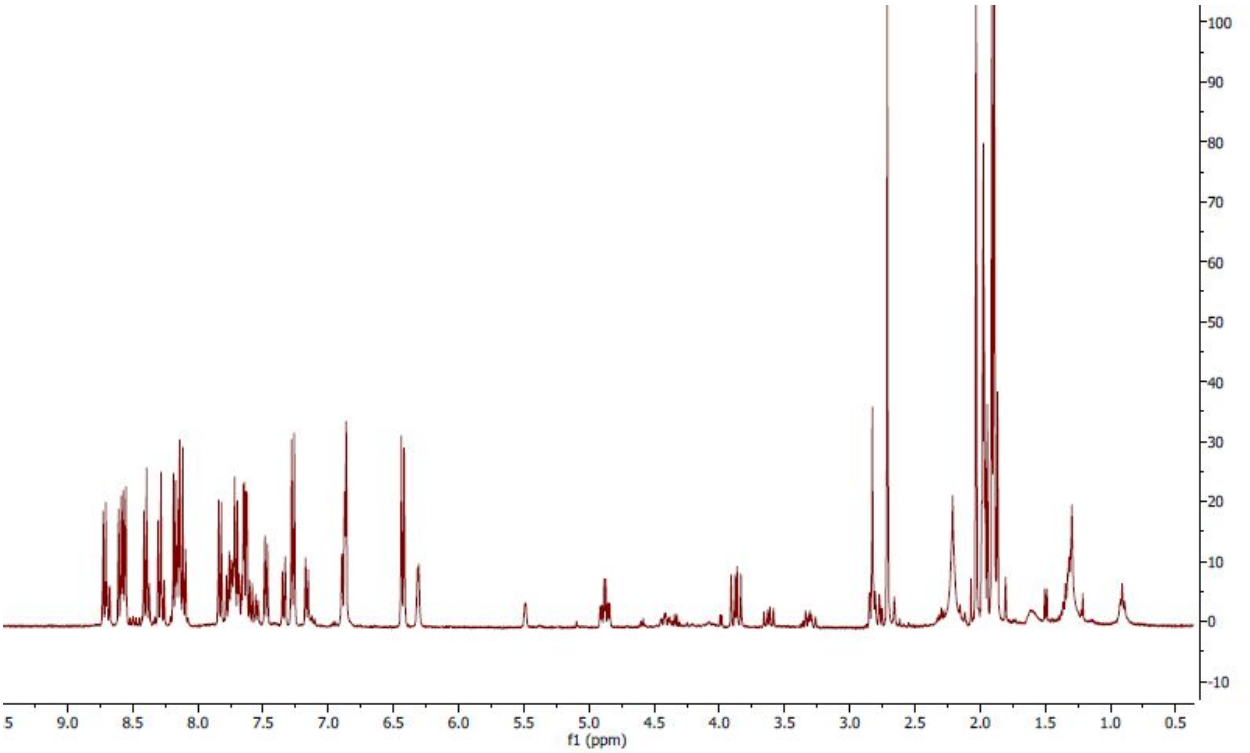

Figure S22. ^{1}H NMR of **2** in CD_3CN.

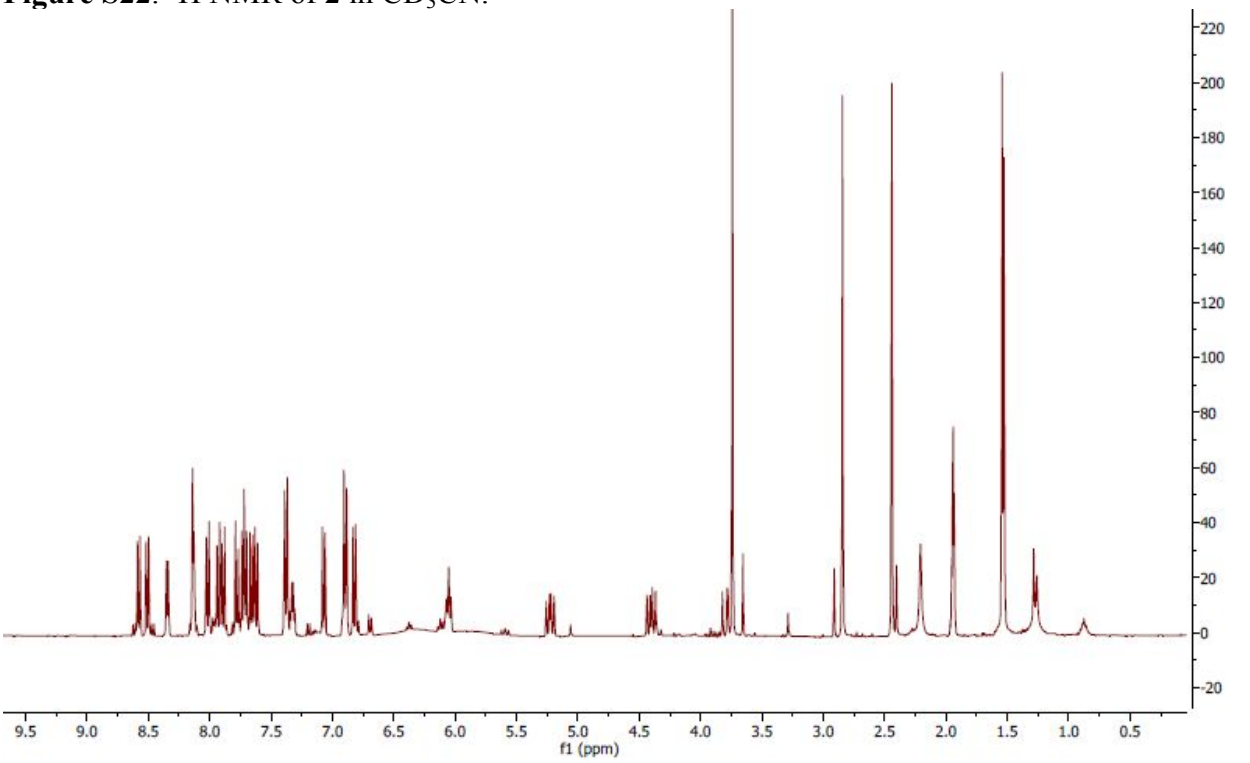

Figure S23. ^{1}H NMR of **3** in CD_3CN.

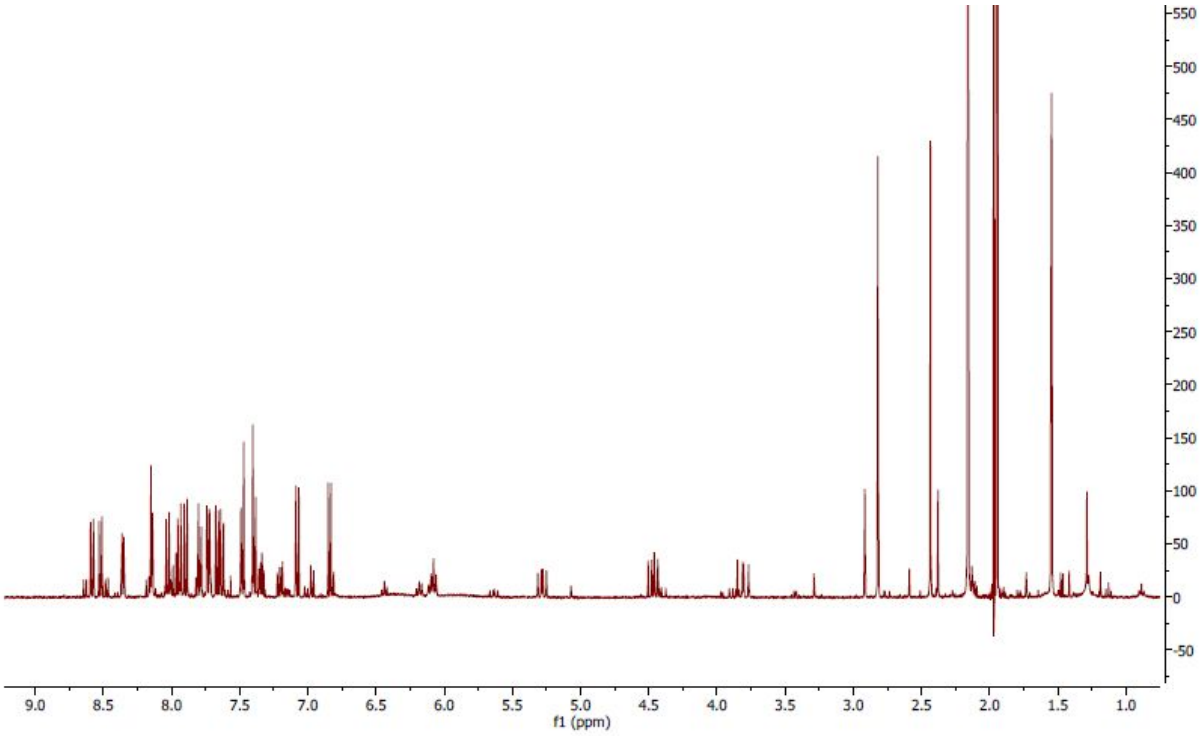

Figure S24. ^{1}H NMR of **4** in CD_3CN.

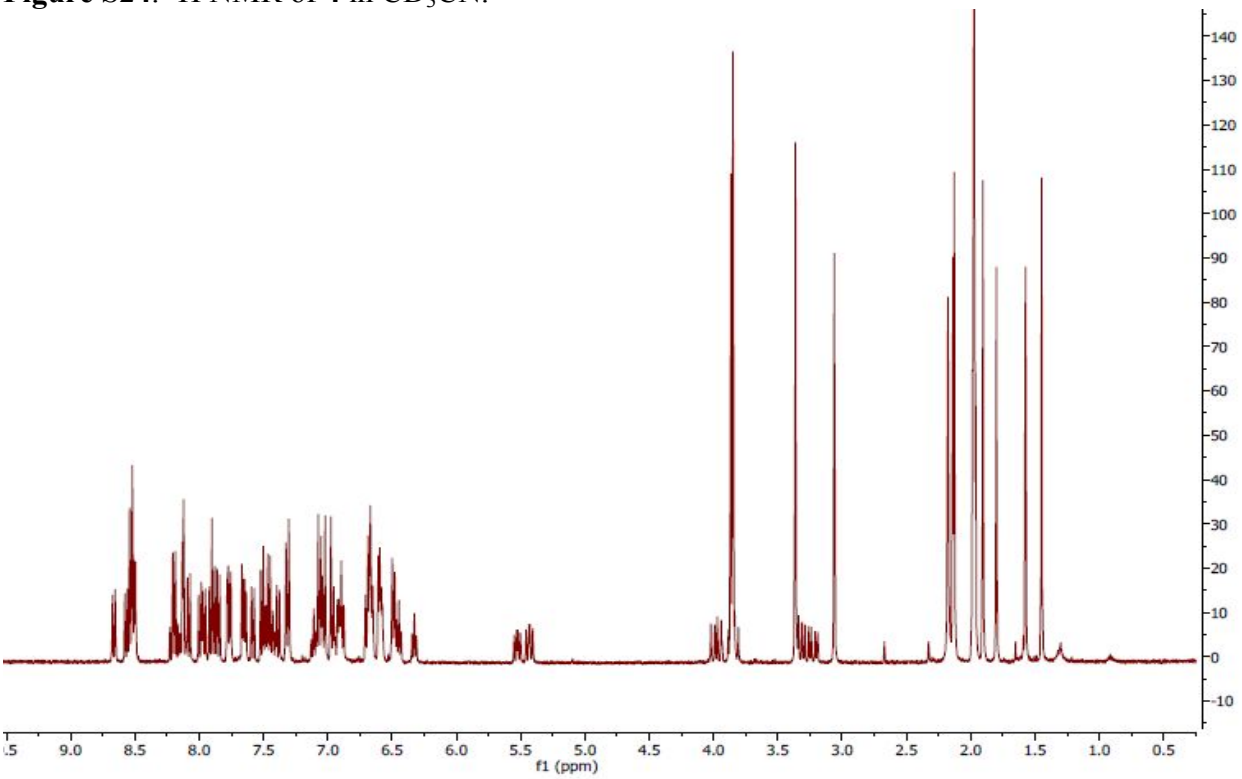

Figure S25. ^{1}H NMR of **5** in CD_3CN.

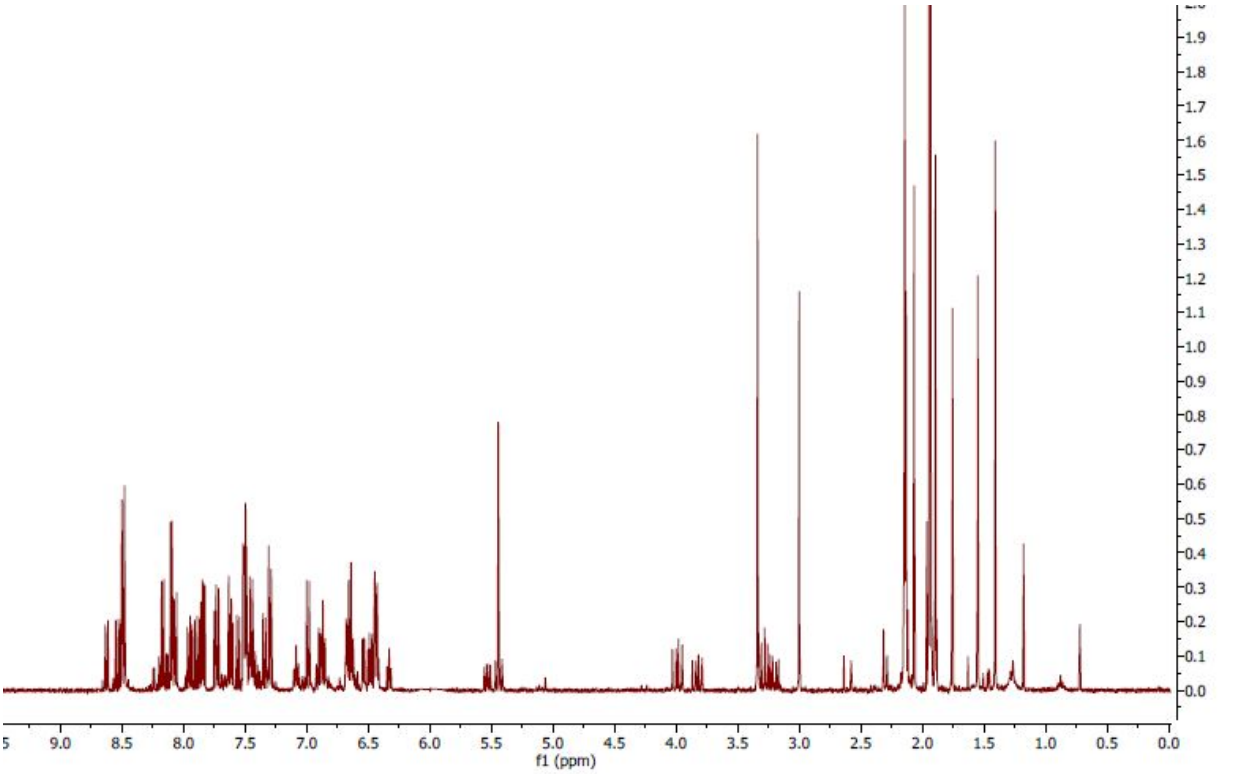

Figure S26. ^{1}H NMR of **6** in CD_3CN.

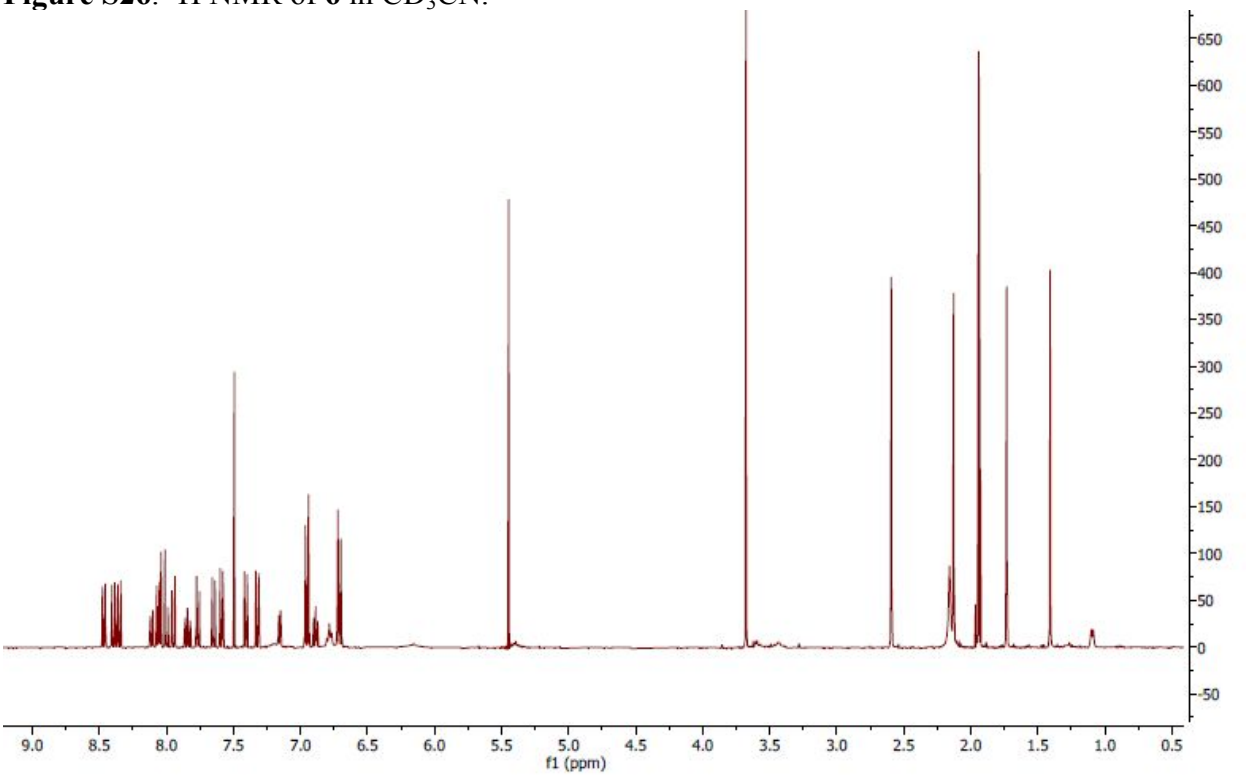

Figure S27. ^{1}H NMR of **7** in CD_3CN.

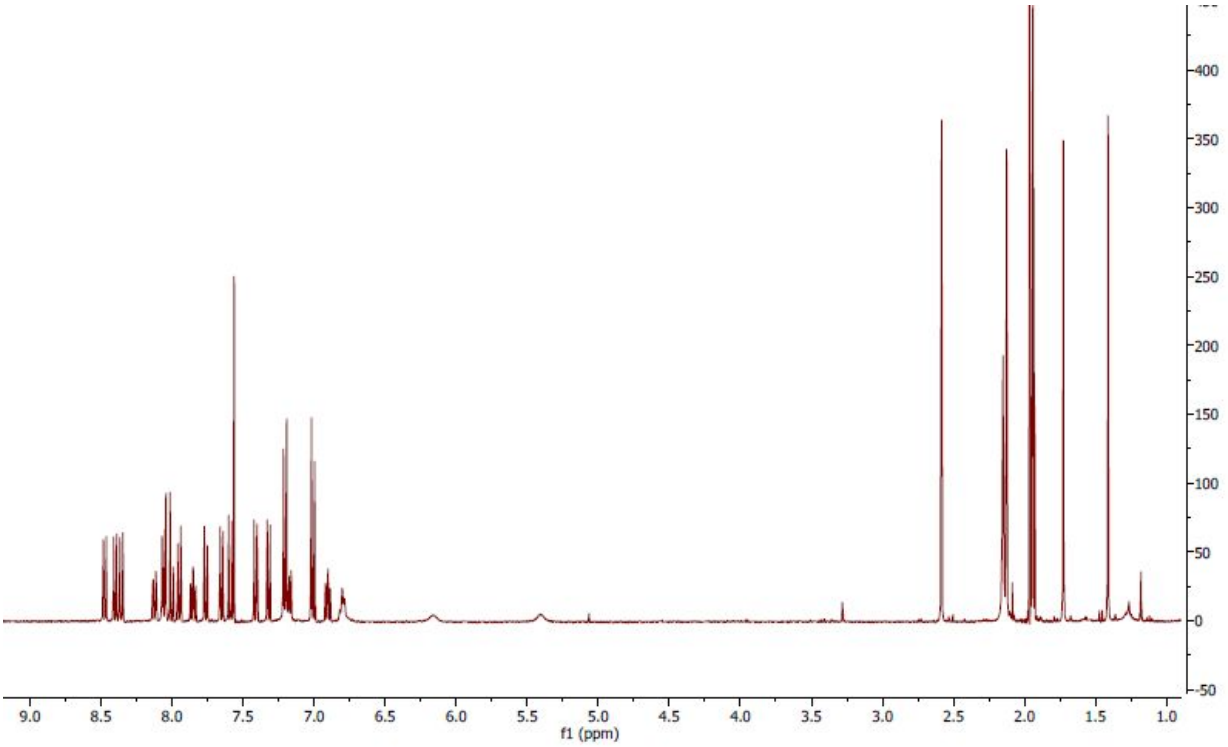

Figure S28. ^{1}H NMR of **8** in CD_3CN.

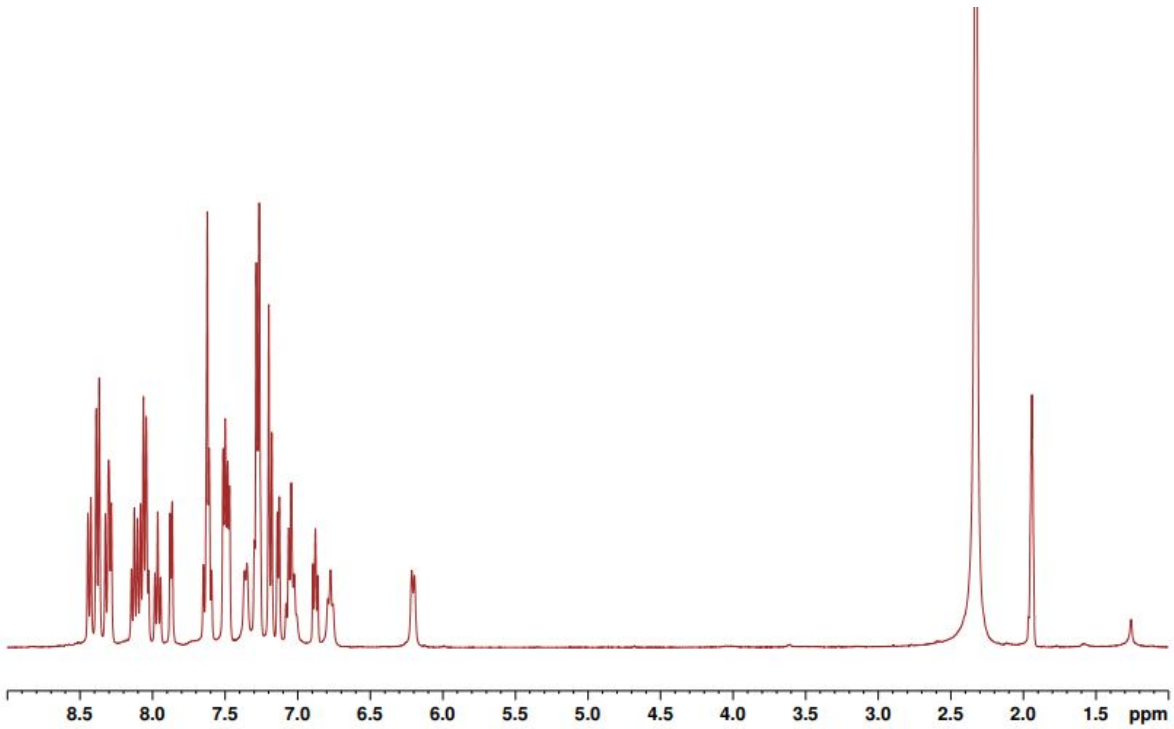

Figure S29. ^{1}H NMR of **9** in CD_3CN.

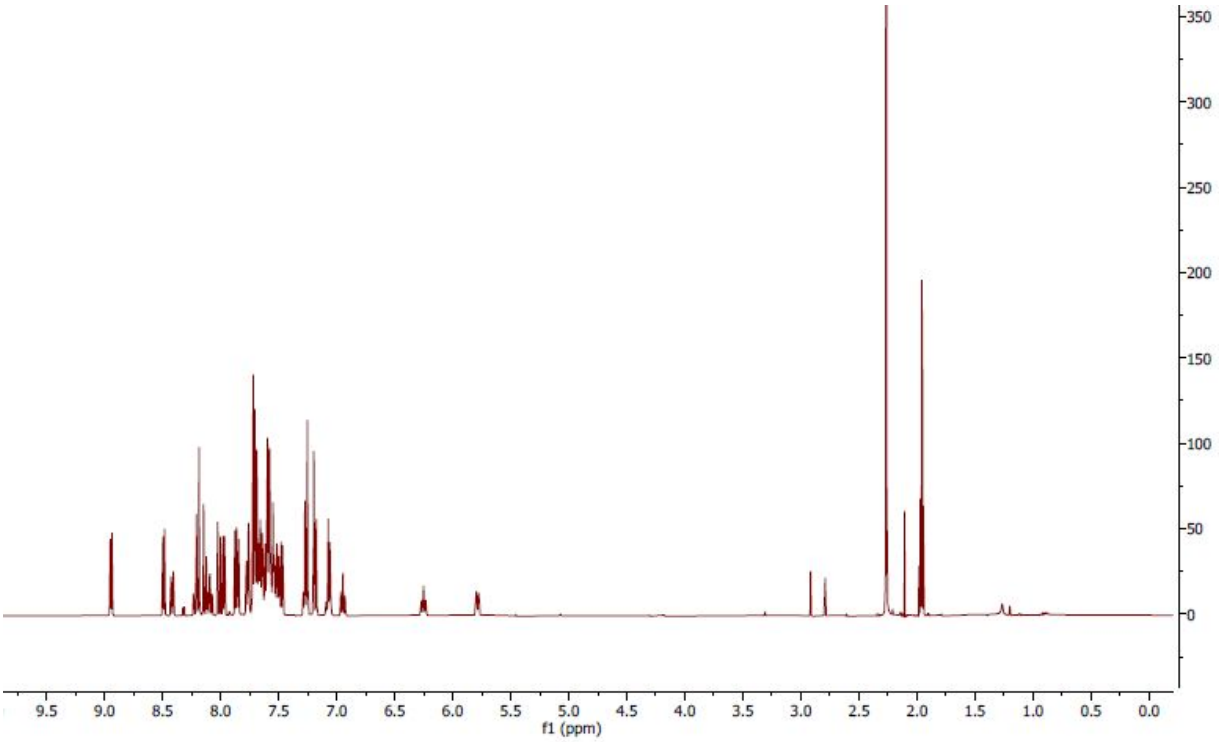

Figure S30. ^{1}H NMR of **10** in CD_3CN.

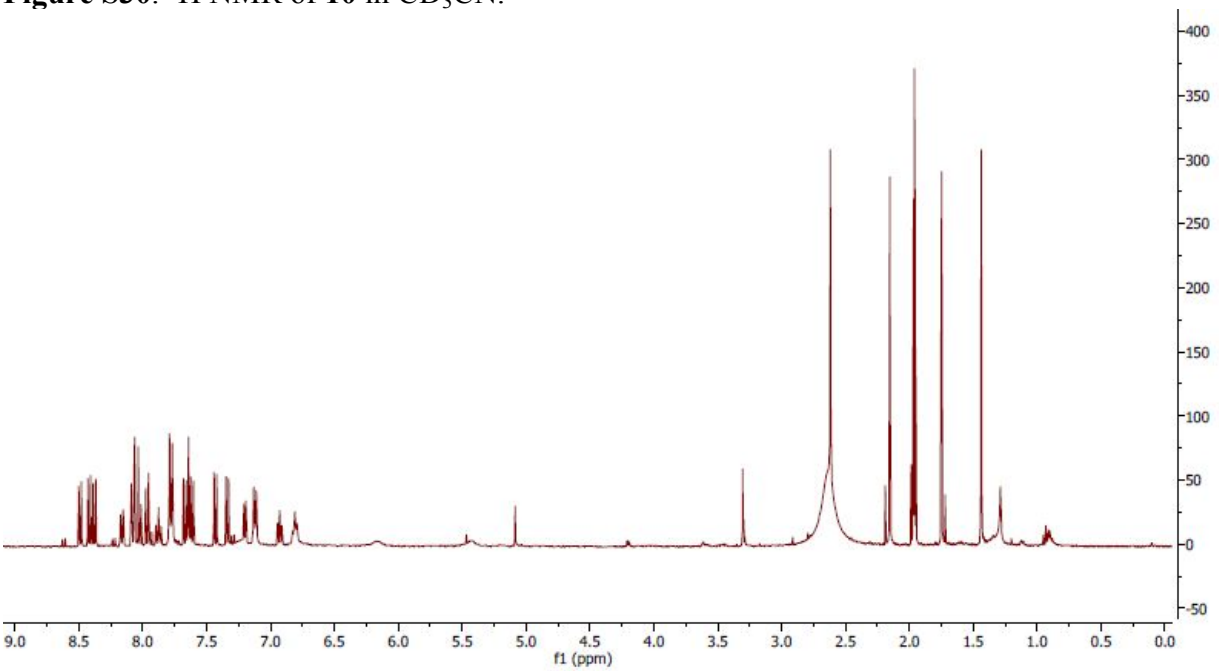

Figure S31. ^{1}H NMR of **11** in CD_3CN.

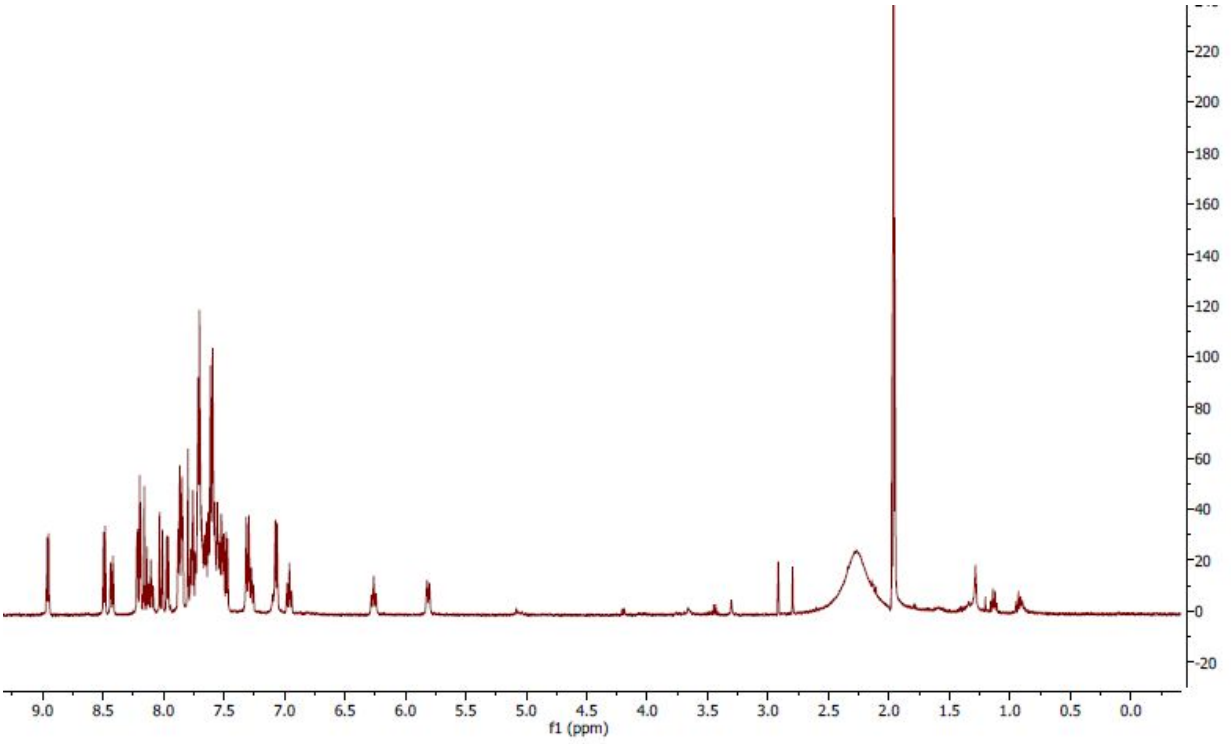

Figure S32. ^{1}H NMR of **12** in CD_3CN.

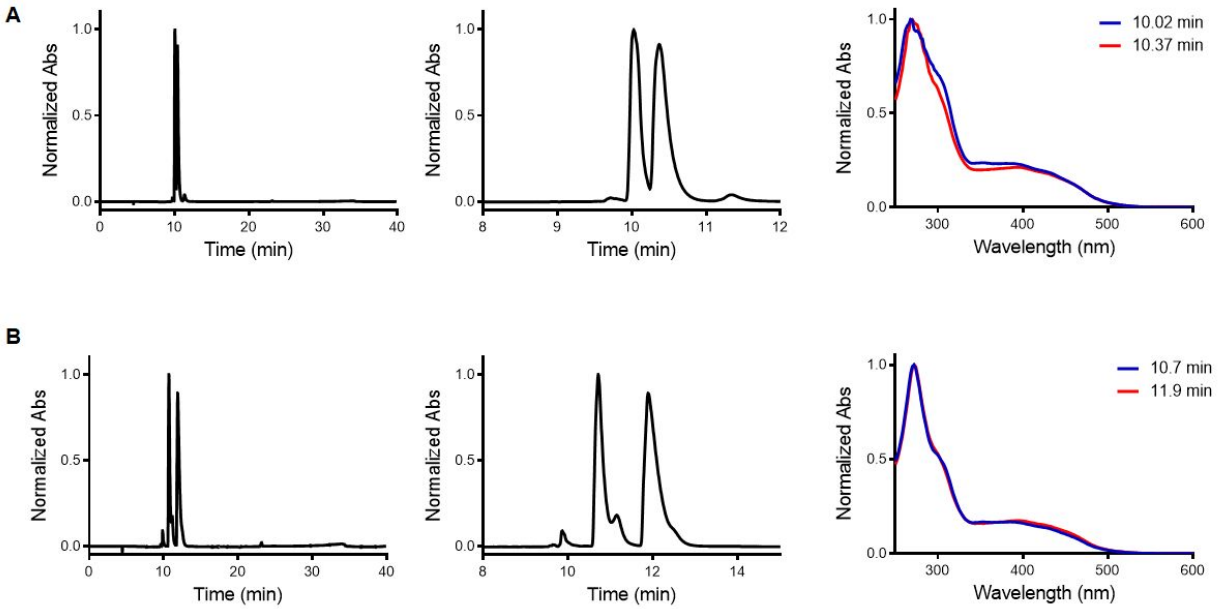

Figure S33. HPLC chromatograms of **5** (A) and **6** (B) with expansion (middle) and absorption profile (right) indicating the separation of diastereomers on a reverse phase C18 100 Å column.

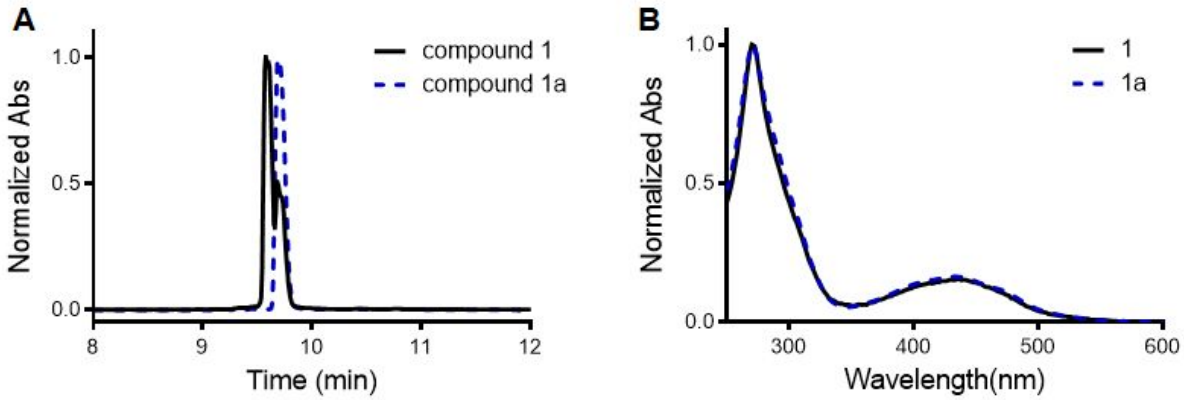

Figure S34. HPLC chromatograms of **1** and **1a** (A) and absorption profile (B) of minor peak for compound **1** compared with compound **1a** indicating an oxidation of pyrazoline unit.

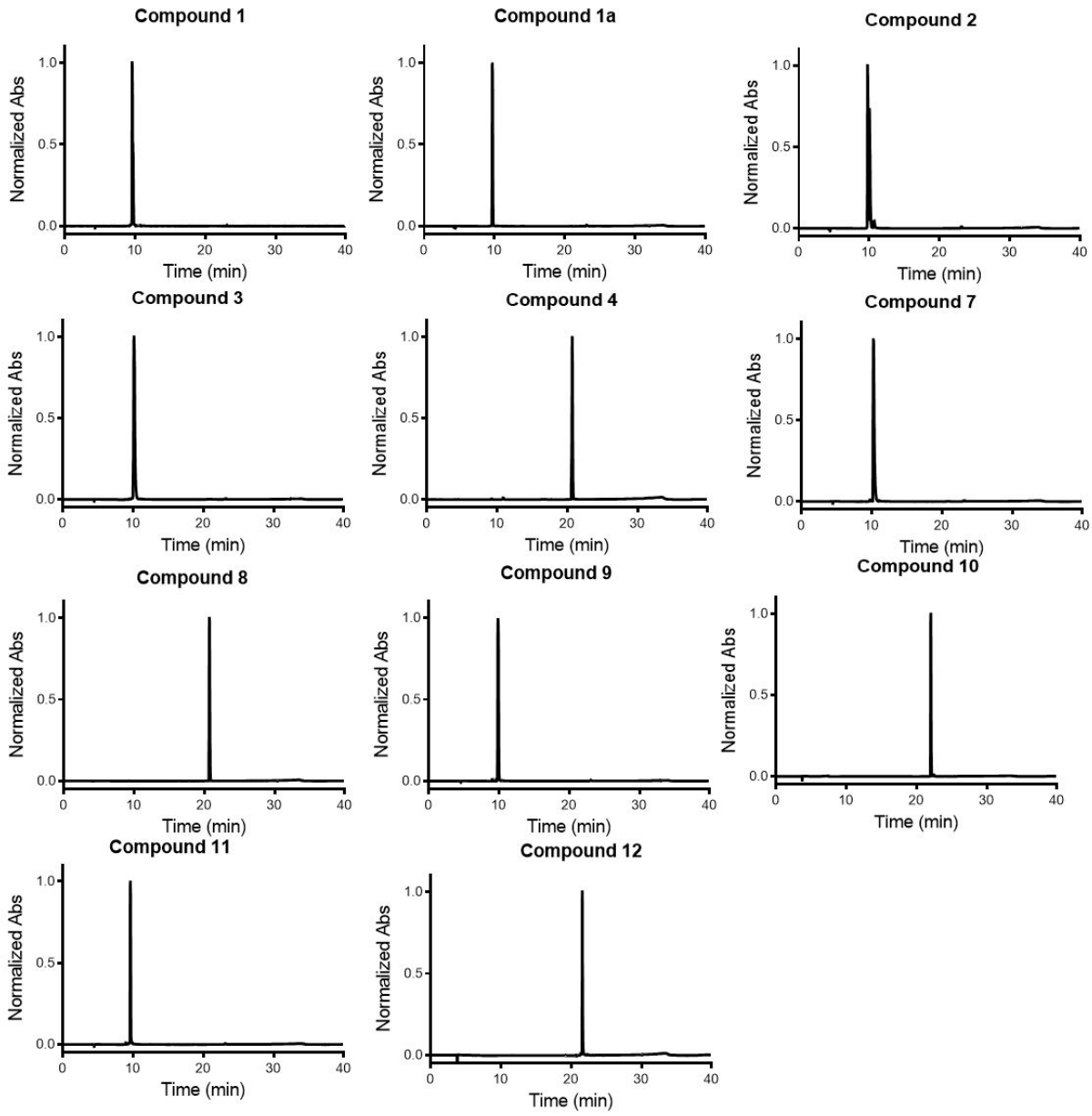

Figure S35. HPLC chromatogram for **1–4**, and **7–12.** Chromatographic conditions were optimized on a Column Technologies Inc. C18 120 Å column (**4**, **8**, **10** and **12**) or Phonomenex Luna 5 µm C18(2) 100 Å (**1–3**, **6**, **7**, and **11**). Detection wavelength of 280 nm.

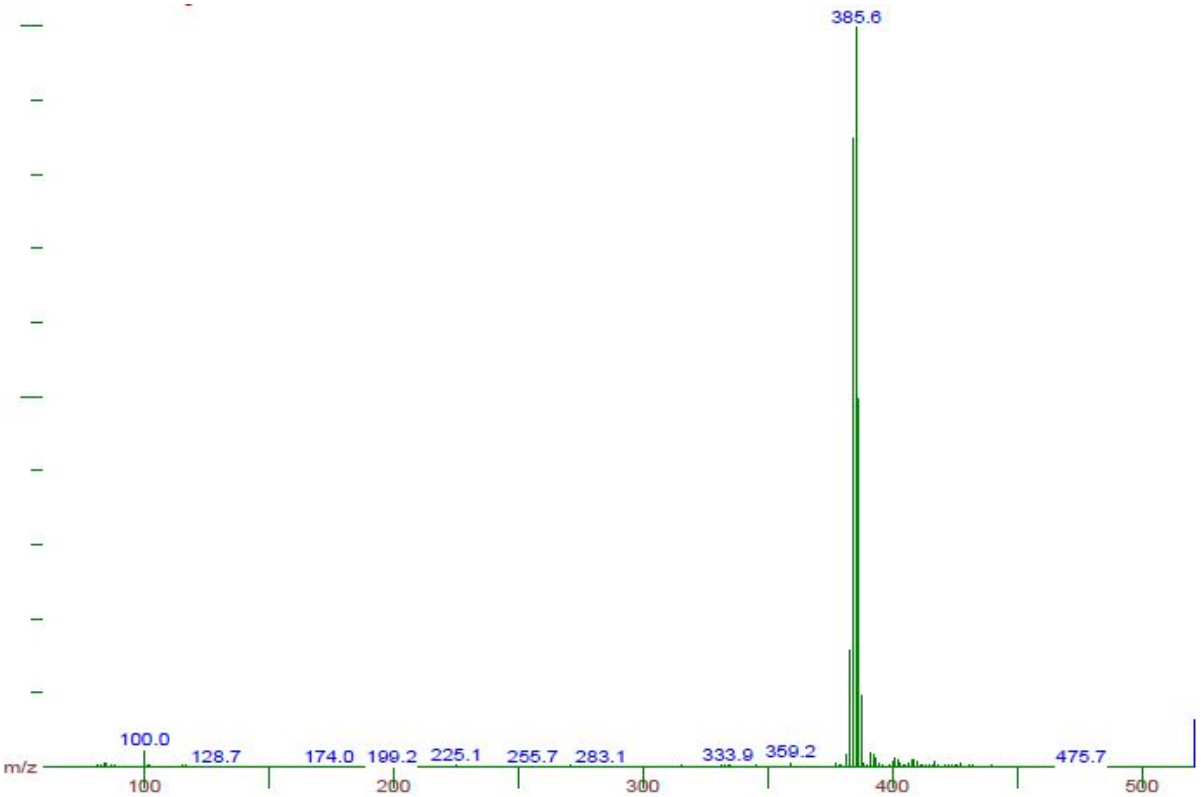

Figure S36. ESI MS of complex **1**, calcd for $C_{43}H_{39}N_7ORu$ $[M]^{2+}$ 385.62; found 385.6 $[M]^{2+}$.

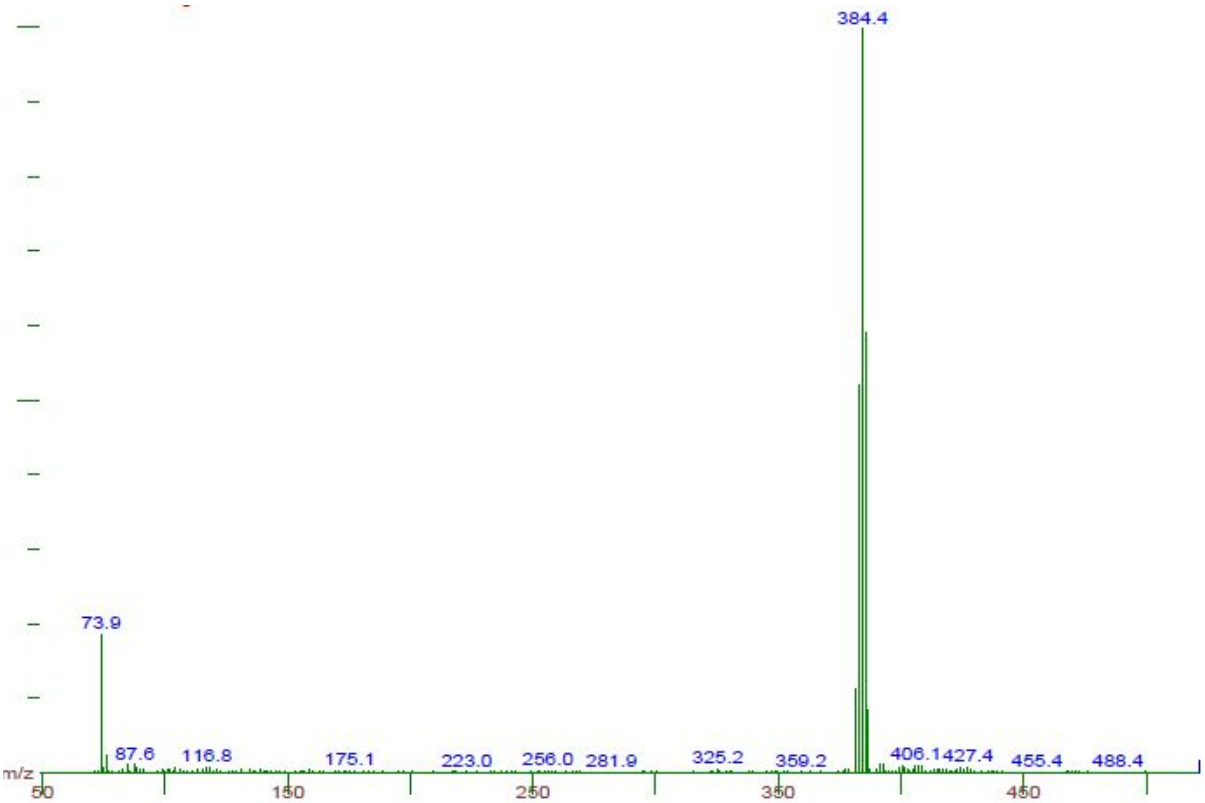

Figure S37. ESI MS of complex **1a**, calcd for $C_{43}H_{37}N_7ORu$ $[M]^{2+}$ 384.61; found 384.4 $[M]^{2+}$.

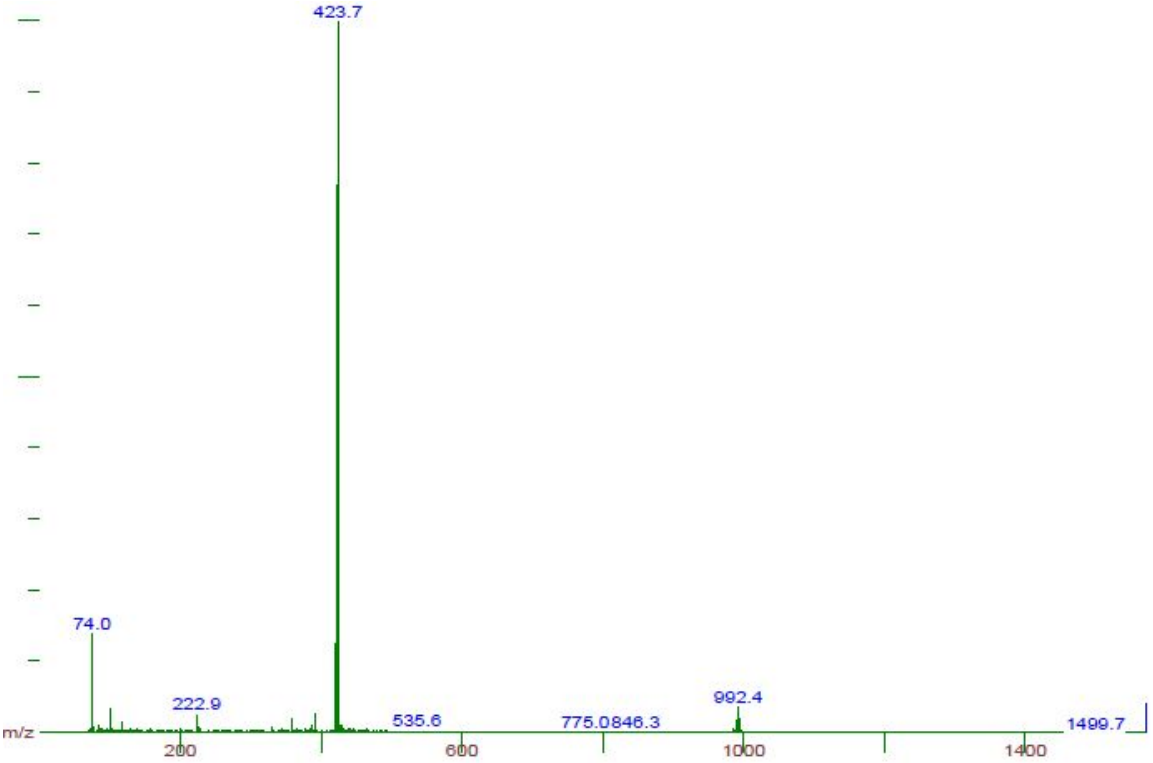

Figure S38. ESI MS of complex **3**, calcd for $C_{49}H_{43}N_7ORu$ $[M^{2+}•PF_6^-]^+$ 992.22, $[M]^{2+}$ 423.63; found 992.4 $[M^{2+}•PF_6^-]^+$, 423.7 $[M]^{2+}$.

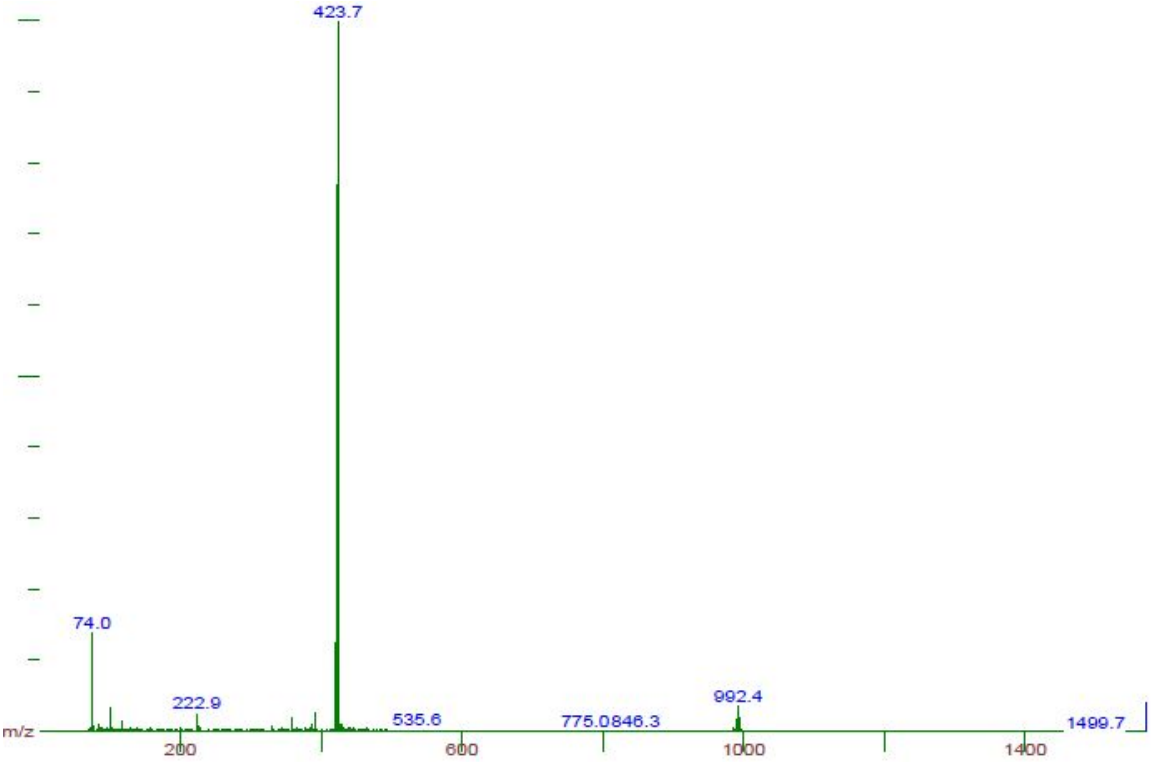

Figure S39. ESI MS of complex **5**, calcd for $C_{49}H_{43}N_7ORu$ $[M^{2+}•PF_6^-]^+$ 992.22, $[M]^{2+}$ 423.63; found 992.3 $[M^{2+}•PF_6^-]^+$, 423.7 $[M]^{2+}$.

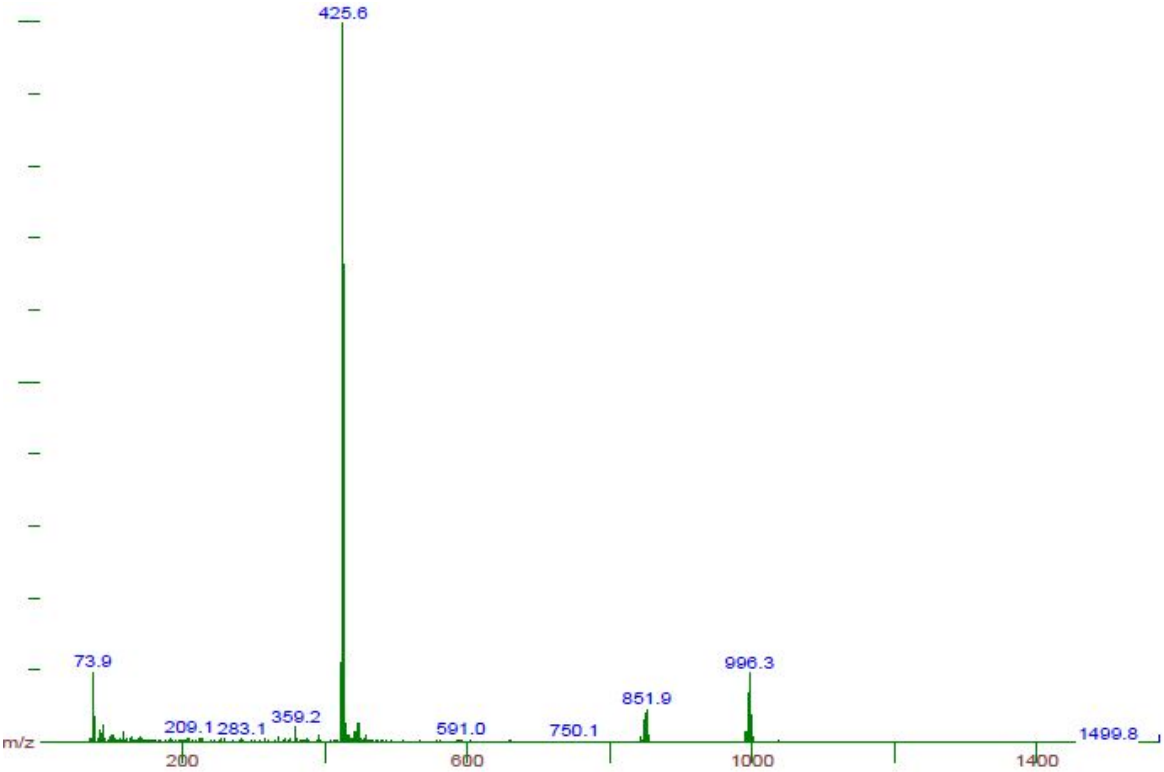

Figure S40. ESI MS of complex **6**, calcd for $C_{48}H_{40}ClN_7Ru$ $[M^{2+}•PF_6^-]^+$ 996.17, $[M]^{2+}$ 425.61; found 996.3 $[M^{2+}•PF_6^-]^+$, 425.6 $[M]^{2+}$.

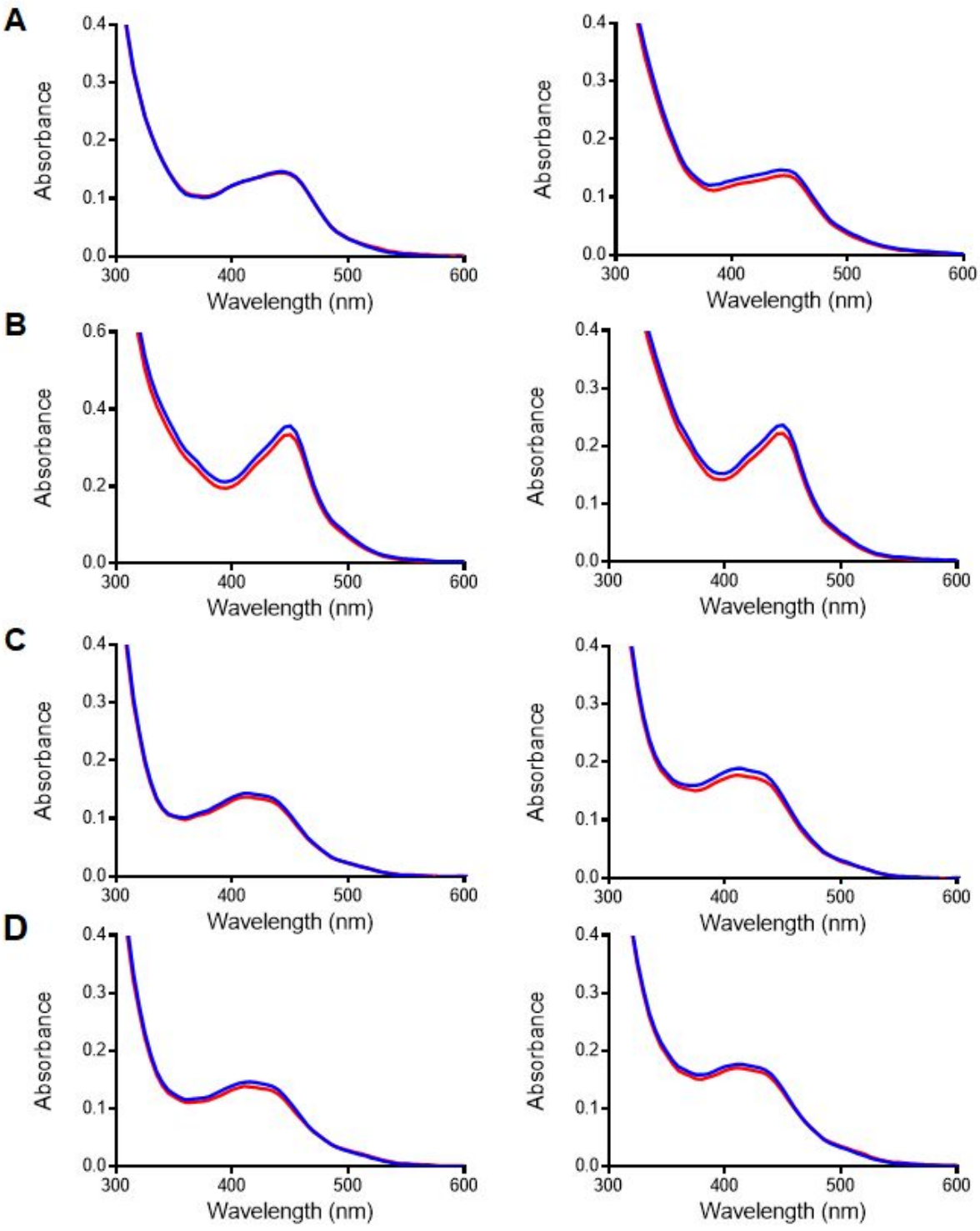

Figure S41. Stability of complexes **2** (A), **4** (B), **8** (C), and **7** (D) in water (left) and Opti-MEM (right) at 37 °C in the dark over the course of 0 (blue line) to 72 h (red line), followed by UV/vis absorption.

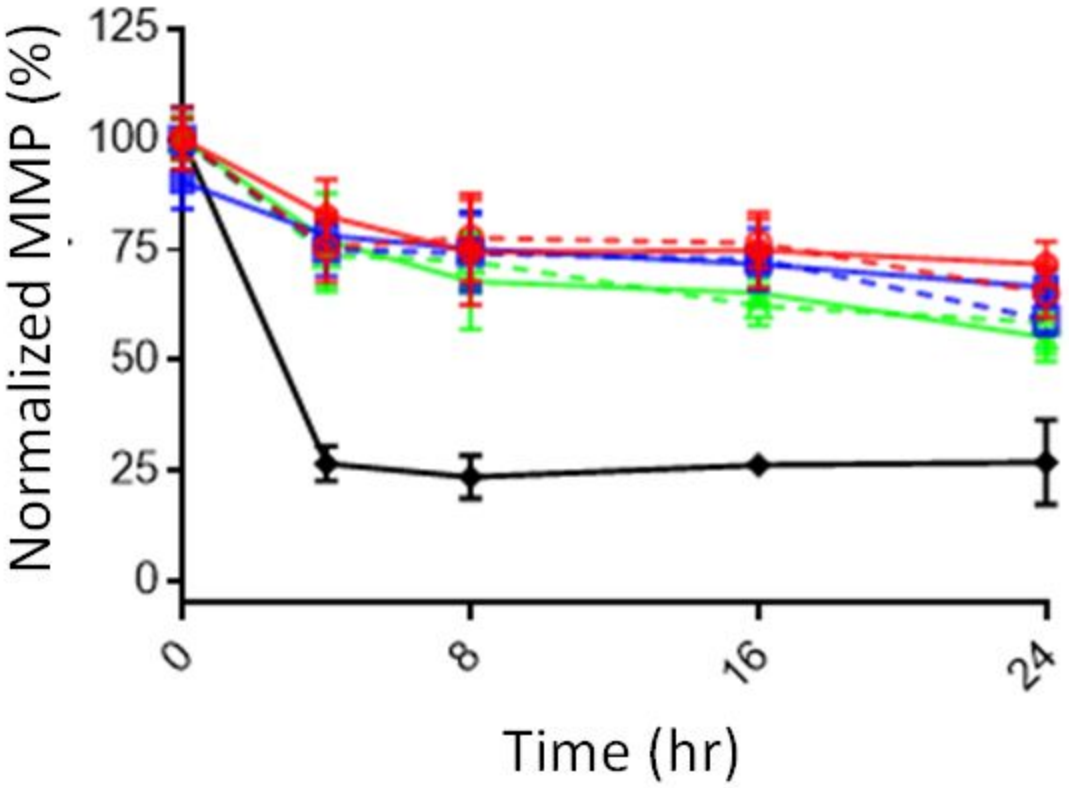

Figure S42. Time dependent inhibition of mitochondrial function with complexes **2** (red), **4** (blue), and **8** (green) upon dark (solid) and light (dashed) condition compared with control compound (carbonyl cyanide 3-chlorophenylhydrazone, CCCP, grey).